Biophysical Journal Volume 105 December 2013 2832–2842

An Integrated Mitochondrial ROS Production and Scavenging Model: Implications for Heart Failure

Laura D. Gauthier,[†*] Joseph L. Greenstein,[†] Brian O'Rourke,[‡] and Raimond L. Winslow[†]

[†]Institute for Computational Medicine and Department of Biomedical Engineering, The Johns Hopkins University School of Medicine and Whiting School of Engineering, Baltimore, Maryland; and [‡]Division of Cardiology, Johns Hopkins University School of Medicine, Baltimore Maryland

ABSTRACT It has been observed experimentally that cells from failing hearts exhibit elevated levels of reactive oxygen species (ROS) upon increases in energetic workload. One proposed mechanism for this behavior is mitochondrial Ca^{2+} mismanagement that leads to depletion of ROS scavengers. Here, we present a computational model to test this hypothesis. Previously published models of ROS production and scavenging were combined and reparameterized to describe ROS regulation in the cellular environment. Extramitochondrial Ca^{2+} pulses were applied to simulate frequency-dependent changes in cytosolic Ca^{2+}. Model results show that decreased mitochondrial Ca^{2+}uptake due to mitochondrial Ca^{2+} uniporter inhibition (simulating Ru360) or elevated cytosolic Na^+, as in heart failure, leads to a decreased supply of NADH and NADPH upon increasing cellular workload. Oxidation of NADPH leads to oxidation of glutathione (GSH) and increased mitochondrial ROS levels, validating the Ca^{2+} mismanagement hypothesis. The model goes on to predict that the ratio of steady-state $[H_2O_2]_m$ during 3Hz pacing to $[H_2O_2]_m$ at rest is highly sensitive to the size of the GSH pool. The largest relative increase in $[H_2O_2]_m$ in response to pacing is shown to occur when the total GSH and GSSG is close to 1 mM, whereas pool sizes below 0.9 mM result in high resting H_2O_2 levels, a quantitative prediction only possible with a computational model.

INTRODUCTION

Oxidative stress has been shown in patients experiencing heart failure (HF) through elevated levels of biomarkers in the bloodstream and pericardial fluid (1–3). In animal models of HF, oxidative stress is also present and has been proposed to be a consequence of both increased mitochondrial reactive oxygen species (ROS) production (4) and decreased antioxidant capacity (5–7). Moreover, expression of a mitochondrially targeted H_2O_2 scavenger enzyme, catalase, has been shown to attenuate age-related cardiac dysfunction, oxidative damage, and mortality (8).

Frequent changes in heart rate equating to changes in cardiac workload require tight regulation of ATP supply and demand. This regulation of ATP is carried out by ADP and Ca^{2+} signals. Experimental data shows that changes in $[Ca^{2+}]_i$ and $[ADP]_i$ induced by changes in pacing frequency exert differing control on the mitochondrial NADH redox state, sometimes referred to as push and pull, respectively. Increases in cytosolic ADP (pull conditions) are conveyed to the mitochondria via the adenine nucleotide transporter and activation of the ATP synthase, which stimulates the respiratory rate and oxidizes NADH. At the same time, increased cytosolic Ca^{2+} transients lead to increased mitochondrial Ca^{2+} via the mitochondrial Ca^{2+} uniporter (mCU). Elevated mitochondrial Ca^{2+} stimulates the Ca^{2+}-sensitive enzymes of the tricarboxylic acid (TCA) cycle, leading to enhanced production of NADH. These two complementary processes serve to maintain homeostasis of NADH redox potential so that mitochondrial energy production can be maintained. NADH levels in the mitochondrial matrix are linked to NADPH levels through the proton-translocating transhydrogenase (THD). Nicotinamide adenine dinucleotide phosphate (NADPH) can also be produced in the matrix by the actions of the $NADP^+$-dependent isocitrate dehydrogenase and malic enzyme, two enzymes that also depend on TCA cycle intermediates. NADPH plays a critical role in maintaining antioxidant capacity through the NADPH-dependent enzymes glutathione reductase (GR) and thioredoxin reductase (TrxR), maintaining the reduced state of the glutathione (GSH) and thioredoxin (Trx) antioxidant pools, which are oxidized as a consequence of H_2O_2 scavenging by glutathione peroxidase and peroxiredoxin, respectively. $[Ca^{2+}]_m$ thus plays a key role in regulating mitochondrial ROS scavenging through coupling between the generation of redox equivalents for energy generation and the antioxidant pathways.

Cytosolic Na^+ levels have been shown to be elevated in HF (9–11), and contribute to mitochondrial ROS production (12–14). Elevated cytosolic Na^+ increases the rate of the mitochondrial Na^+-Ca^{2+} exchanger (mNCE), which promotes mitochondrial Ca^{2+} efflux and decreases the mitochondria's ability to accumulate Ca^{2+} during pacing. Without Ca^{2+}-induced TCA cycle stimulation, NADH and NADPH become more oxidized and are unable to recharge the antioxidant systems, which is hypothesized to lead to the high ROS emission seen in HF cells at high pacing frequencies (15). This proposed mechanism of energy

---

Submitted July 19, 2013, and accepted for publication November 5, 2013.

*Correspondence: laura.doyle@jhu.edu

Editor: Robert Nakamoto.

0006-3495/13/12/2832/11 $2.00

http://dx.doi.org/10.1016/j.bpj.2013.11.007

insufficiency in HF emphasizes the importance of Ca^{2+} signaling at the cellular and mitochondrial levels.

Previous work (16,17) has endeavored to demonstrate the impact of variations in scavenging capacity on observed ROS overflow from mitochondria. Although the models furthered the understanding of the contribution of ROS scavenging to ROS overflow, none of them included a physiological model of ROS production. Several models of ROS production exist (18–25), each having various strengths and weaknesses. We recently developed a model of ROS production (25) that constrained respiratory rate, electron transport chain (ETC) redox state, and ROS production rates from complexes I and III using experimental data. This model of ROS production was chosen as a module for the model presented here because of its extensive validation using experimental data from cardiac mitochondria wherever possible. In this work we combine detailed models of ROS scavenging and ROS production to understand how these two mechanisms control ROS levels in HF.

METHODS

Model description

Fig. 1 depicts the components of the cardiac ROS production and scavenging pathways represented in the model. Briefly, the electron transport chain with ROS production comes from the Gauthier et al. (25) electron transport chain and reactive oxygen species (ETC-ROS) model. The only modifications were scaling ROS production to agree with experimental data in the absence of scavenging (16) and slight changes to complex I for the cellular model (see the Supporting Material for details). ROS scavenging was derived from the Kembro et al. (17) mitochondrial energetic-redox (ME-R) model with some changes to parameters as noted in the Supporting Material. Both of these models represent guinea pig cardiac mitochondria and were fit to data from such preparations wherever possible.

Computational methods

The mitochondrial model introduced here consists of 37 nonlinear ordinary differential equations. The equations were implemented in MATLAB 7.1 (The MathWorks, Natick, MA). Model parameters were optimized using the fmincon function from MATLAB. For the protocols described, the model was run from steady-state resting initial conditions, when the magnitude of each time derivative was $\leq 10^{-5}$ mM/ms. Initial conditions are given in the Supporting Material.

Model integration

The ETC-ROS model was successfully incorporated into the ME-R isolated mitochondria model with minimal changes. It was necessary to add explicit dependence on succinate and malate and inhibition by oxaloacetate to the equation for succinate dehydrogenase to couple the enzyme to the TCA cycle. ROS production rates were scaled to match those of the ME-R model. The behavior of isolated mitochondria is often compared between state 4 respiration (energized with substrates, but in the absence of ADP) and state 3 respiration (energized with substrates in the presence of ADP) to deduce the effects of rapid respiration rates associated with ATP production in state 3. A comparison of state 4 and state 3 steady-state behaviors from experimental data, the ME-R model, and the combined ME-R and ETC-ROS model are presented in Table 1.

A significant achievement of this model is that ROS production is modulated between state 3 and state 4 without a change in the model parameters. This is also evident in Fig. S1 in the Supporting Material showing the effect of inhibition of the GSH or Trx scavenging systems in state 3 and state 4. The present model maintains the proportional control established by Kembro et al. (17) such that inhibition of the Trx system leads to higher H_2O_2 emission fluxes than inhibition of the GSH system, as has been shown experimentally for guinea pig (17). The dynamics of the ME-R model were also maintained after incorporation of the ETC-ROS model. See Fig. S2 for the comparison of substrate and

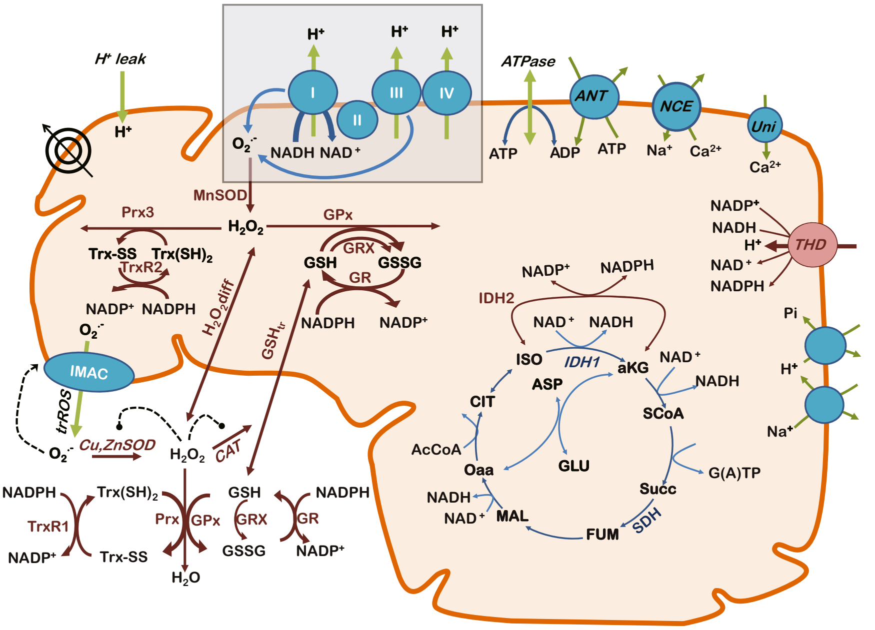

FIGURE 1 Overview of the mitochondrial model, including ROS production and scavenging pathways. The model presented here builds upon the model of Kembro et al. (17) by incorporating a detailed, mechanistic model of the ETC (*gray box*) by Gauthier et al. (25) that determines respiratory and superoxide production fluxes. The combined model features mechanistic ROS production from the ETC, mitochondrial matrix scavenging, transport of H_2O_2 across the inner mitochondrial membrane, extramitochondrial scavenging, NADH, and NADPH production by the TCA cycle, NAD^+/NADH and $NADP^+$/NADPH interconversion by THD, and mitochondrial ion handling. For simulations of cellular behavior, the extramitochondrial space represents the cytosol. See the Supporting Material for specific parameter changes. To see this figure in color, go online.

TABLE 1 Quantitative comparison of energetic measurements in the absence of scavenging

	Experimental		Kembro et al. model		New model	
Variable	St 4	St 3	St 4	St 3	St 4	St 3
Respiration (nmol/mg protein/min)	46 ± 2.6	152 ± 8.5	27.92	58.52	34.78	59.41
H_2O_2 emission (nmol/mg protein/min)	0.56 ± 0.01	0.48 ± 0.06	0.48	0.46	0.2582	0.1949
H_2O_2 emission as % of respiratory flux	0.74	0.29	1.7	0.78	0.74	0.33
$\Delta\Psi_m$ (mV)	167 ± 7	142 ± 2	192.5	168	194.5	168.9
NADH (%)	98 ± 4	78 ± 5	96.5	61.3	94.6	65.2

Energetic and ROS-related measurements are compared across experimental data from Aon et al. (16), the Kembro et al. model (17), and the model presented here. For simulations state 4 ADP = 0.01 mM and state 3 ADP = 1.0 mM. Kembro et al. (17) data were simulated from code supplied by the authors. The shunt value for that code was 0.018 for state 4 and 0.008 for state 3. A scale factor of 2 × 60e3 was used to convert from mM/ms to nmol/min/mg protein.

ADP addition protocols before and after the incorporation of the ETC-ROS model.

Parameter fitting for mitochondrial model in the myocyte

The ROS scavenging model introduced in Kembro et al. (17) was originally parameterized to reproduce steady-state ROS emission data from isolated mitochondria. To reproduce kinetic data on ROS emission from isolated myocytes, some parameters were refit. Isocitrate dehydrogenase $NADP^+$ (IDH2) was refit using in vitro parameters from Popova et al. 2007 (26). The random bi-bi enzyme kinetics model describing the activity of the THD based on the randomly ordered binding of two substrates and the randomly ordered unbinding of two products presented in Kembro et al. (17) was modified to satisfy the thermodynamic constraint from Sazanov and Jackson (27). Kinetic parameters for glutathione peroxidase were refit to improve GSH sensitivity as compared to GSH-dependence data from Aon et al. 2010 (28) (their Fig. 10 *D*). The Michaelis-Menten constant of glutathione reductase for NADPH was increased to improve sensitivity over the range of observed NADPH values in the model. Other model parameters were modified to better represent the conditions of the mitochondria in isolated myocytes. Refer to the Supporting Material for more details.

Stimulus protocols

During pacing, the mitochondrial model was subjected to changes of extra-mitochondrial Ca^{2+} and ADP concentrations to simulate a change in energetic workload stimulated by the increased demand for ATP during contraction. $[Ca^{2+}]_i$ transients were simulated as rectangular pulses of Ca^{2+} from a diastolic level of 0.1–1 μM with a width of 200 ms. Cytosolic ADP was increased from a basal level of 0.1–1.0 mM with a time constant of 2 min to simulate the energy consumption by the contractile machinery in the cytosol. Isoproterenol was present in the experiments used for comparison to accelerate the increase of $[Ca^{2+}]_i$ transient peaks from rest to the steady-state pacing value near 1 μM. The effects of isoproterenol were not explicitly simulated in the model other than to use the 1 μM value for peak cytosolic Ca^{2+}. For the myocyte model simulations, pH and mitochondrial phosphate were held constant.

RESULTS

Altered Ca^{2+} regulation by Ru360 increases ROS

A comparison of model behavior from rest to 3Hz pacing, with or without 90% uniporter block (to simulate Ru360, a mCU blocker), is shown in Fig. 2, along with experimental

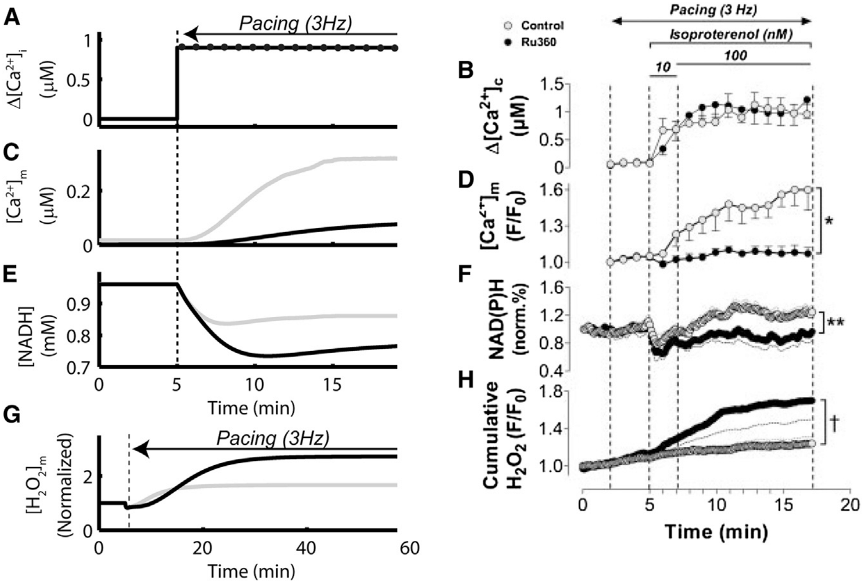

FIGURE 2 Ru360 inhibits Ca^{2+} uptake, decreases NADH supply, and increases H_2O_2 release at high workloads. (*A*) Model cytosolic Ca^{2+} was held constant at 0.1 μM before pacing and simulated after the onset of pacing as 200 ms periodic pulses of 1 μM from a resting level of 0.1 μM. (*B*) Experimental $[Ca^{2+}]_i$ transients exhibit similar values before pacing and after the addition of isoproterenol. (*C*) Control $[Ca^{2+}]_m$ in the model accumulates to over 0.3 μM for control (*gray*), whereas uniporter block limits accumulation to below 0.1 μM for the first 15 min of pacing (*black*). (*D*) Fluorescence signal for $[Ca^{2+}]_m$ shows similar kinetics to model data. (*E*) In simulations, uniporter inhibition (*black*) results in more extensive oxidation of NADH than for control (*gray*) resulting in 0.86 mM NADH after 15 min pacing for control compared to 0.77 mM for mCU inhibition. (*F*) Experimental NADH for Ru360 (*solid symbols*) is ~80% oxidized during pacing with control NADH (*open symbols*) recovering to levels higher than at rest. (*G*) Although an increase in workload elevates mitochondrial $[H_2O_2]$ for both control (*gray*) and uniporter block (*black*) simulations, ROS for uniporter block conditions is 2.7× higher after pacing than at rest compared to 1.67× for control. (*H*) Experimental data also show elevated $[H_2O_2]$ for Ru360 compared to control, but with faster kinetics. Note that panel (*C*) of simulations shows a longer simulation. Experimental data reproduced from Kohlhaas et al. (15) 90% reduction in mCU flux is used to simulate Ru360 application in the model.

data for the same protocol from Kohlhaas et al. (15). For control conditions, the onset of pacing increases cytosolic transients (Fig. 2, *A - model* and *B - experiment*), which leads to elevation of mitochondrial Ca^{2+}, as shown in the model (Fig. 2 *C*, *gray*) and experiment (Fig. 2 *D*, *open symbols*). However, if mitochondrial Ca^{2+} regulation is altered by a decrease in mCU flux, mitochondrial Ca^{2+} uptake is then severely compromised, as shown in the model (Fig. 2 *C*, *black*) and in experiment (of Fig. 2 *D*, *solid symbols*). In the event of altered Ca^{2+} regulation, NADH control is also compromised. In this case, there is no Ca^{2+}-induced stimulation of the TCA cycle and NADH becomes oxidized, as shown in the model (Fig. 2 *E*, *black*) and in experiment (Fig. 2 *F*, *solid*). As in the experimental data (15) shown in Fig. 2 *F* (*open symbols*), model control NADH levels show only a small variation after the onset of pacing (Fig. 2 *E*, *gray*). In contrast, simulations with mCU inhibition show a significant decline in NADH upon pacing with little to no recovery (Fig. 2 *E*, *black*). Insufficient NADH in the mCU inhibition protocol is associated with increased H_2O_2 over control, as shown in the model (Fig. 2 *G*) and in experiment (Fig. 2 *H*).

NADPH plays a critical role in the mitochondrial scavenging system. As NADH becomes oxidized after the onset of pacing at 5 min (Fig. 2 *E*), THD transfers electrons from NADPH to NAD^+, thus decreasing NADPH levels as shown in Fig. 3 *A*. For simulations with mCU block, the NADH depletion during pacing is larger, leading to a more substantial decrease in NADPH (Fig. 3 *A*, *gray line*). As NADPH levels decrease, the rate of GR activity decreases and GSH becomes more oxidized, as shown in Fig. 3 *B*. A similar mechanism applies to TrxR and Trx (see Fig. S3), though to a lesser degree. It is the decrease in GSH concentration that links the oxidation of NADH to increased ROS release from the mitochondria. As GSH becomes oxidized, the scavenging abilities of the mitochondria are decreased, leading to an accumulation of H_2O_2 in the matrix and a higher rate of release into the cytosol. Note that the GSH redox potentials at rest and during pacing predicted by the model agree well with the 280–250 mV range of GSH redox potential measured experimentally in isolated mitochondria by Aon et al. (28) in response to a similar protocol in which antioxidant depletion increases ROS release (their Fig. 10 *D*).

Development of the isolated ETC-ROS model included validation of steady-state ROS production against different constant NADH levels and $\Delta\Psi$ values obtained from experimental data in isolated mitochondria (25). Results from this previous study show that ROS production increases with $\Delta\Psi$ and with increased reduction of NADH. After this model was incorporated into the dynamically varying mitochondrial environment, Ca^{2+} and ADP transients were applied to simulate pacing. Immediately after the onset of pacing, $\Delta\Psi$ and NADH decreased. The immediate drop in both of these variables leads to an abrupt decrease in ROS production with and without mCU inhibition, according to the model (Fig. 4). As mitochondrial Ca^{2+} increases in control simulations, NADH production is stimulated. Higher NADH concentrations increase the activity of complex I of the ETC, which uses electrons from NADH to reduce ubiquinone (Q) to ubiquinol (QH_2). As the total mitochondrial ubiquinone pool (Q pool) becomes more reduced ROS production is increased, leading to a new, to our knowledge, steady-state level slightly above the resting rate. With decreased Ca^{2+} stimulation of NADH production in the mCU inhibition simulations, the extent of reduction of the Q pool is not as great and steady-state ROS production remains lower than at rest. To observe the increased ROS release for Ru360 shown experimentally, the decrease in scavenging

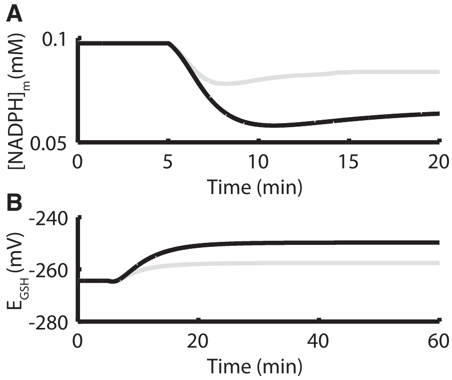

FIGURE 3 mCU inhibition prevents NADPH recovery after onset of pacing, which depletes GSH. (*A*) Model simulations predict that NADPH is ~40% oxidized in the presence of 90% mCU inhibition (*black*), compared to an approximate 20% decrease for control (*gray*). (*B*) Decreases in NADPH drive oxidation of GSH, which is more extensive in the presence of mCU inhibition. GSH redox potentials for mCU inhibition correspond well with the range given in Fig. 10 of Aon et al. 2010 for ROS overflow in isolated mitochondria.

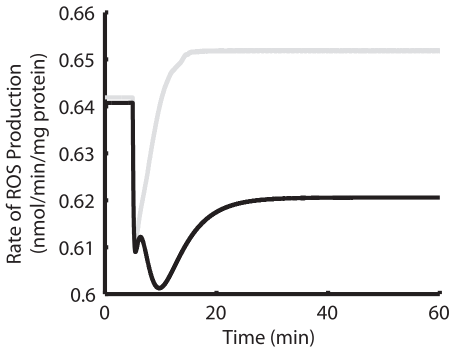

FIGURE 4 Control ROS production increases upon pacing, whereas mCU inhibition causes decrease. Gray line is control and black line is 90% mCU block. For mCU block, $\Delta\Psi$ decreases more upon stimulation than for control. $\Delta\Psi$ has more control over ROS production than NADH in this model. The combination of these two factors and the different rates at which they change also accounts for the complex kinetics between 5 and 10 min.

capacity (see Fig. 3) must outweigh the decrease in ROS production (Fig. 4). This observation helps explain the slow kinetics of model $[H_2O_2]_m$ accumulation under mCU block. Even though GSH oxidation after the onset of pacing reduces scavenging, the drop in ROS production shown in Fig. 4 initially outweighs the decrease in scavenging. However, as GSH continues to oxidize (Fig. 3 *B*) the decrease in scavenging begins to overcome the decrease in ROS production, leading to the slow increase in $[H_2O_2]_m$ shown in Fig. 2 *G*.

Elevated $[Na^+]_i$ alters Ca^{2+} regulation and increases ROS

Cytosolic Na^+ has been experimentally shown to be elevated in both guinea pig models of HF (12) and myocardium from failing human hearts (29). Kohlhaas et al. (15) hypothesized that this may be a key factor in the increased levels of ROS emission observed from myocytes isolated from failing hearts. The mNCE produces a Ca^{2+} extrusion flux that opposes influx through the mCU. In conditions of elevated $[Na^+]_I$, the mNCE rate increases, counteracting the mCU flux and leading to an overall result similar to the block of mCU by Ru360.

Fig. 5 shows simulation results for elevated cytosolic Na^+ compared with experimental results from (15). For control cells, 60 min after the onset of 3Hz pacing, mitochondrial H_2O_2 levels increased 67% in the model (Fig. 5 *A*, *gray*) compared to a 67% increase after 20 min observed in experiments (Fig. 5 *B*, *open symbols*). For cells with cytosolic Na^+ increased to 15 mM, model simulations show a 115% increase in $[H_2O_2]_m$ after 60 min (Fig. 5 *A*, *black*) compared to 148% over 20 min in experiment (Fig. 5 *B*, *solid symbols*). Similar to the mCU inhibition intervention, 15 mM $[Na^+]_i$ leads to compromised mitochondrial Ca^{2+} handling and decreased scavenging capacity (Fig. 6, *A* and *B*, and Fig. S4), which in turn leads to increased mitochondrial H_2O_2. As in the case of mCU inhibition, for elevated $[Na^+]_i$, ROS production is also decreased after the change in workload (Fig. 6 *C*).

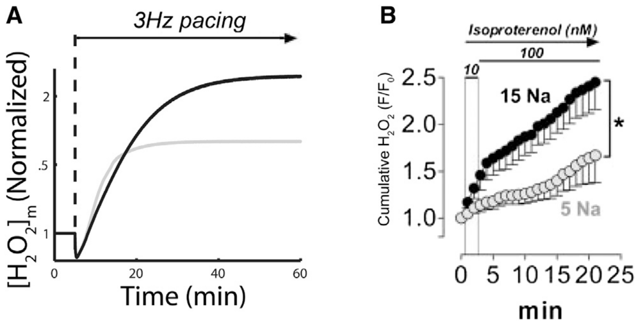

FIGURE 5 Elevated $[Na^+]_i$ increases ROS levels. (*A*) Model cytosolic Na^+ was increased from a control level of 5 mM (*gray*) to 15 mM (*black*), within the range associated with HF. After the onset of 3Hz pacing at 5 min, both simulations show elevated $[H_2O_2]_m$, though high Na^+ continues to increase beyond the steady state for control. (*B*) Experimental data from Kohlhaas et al. (15) show a quantitatively similar trend, though with faster kinetics.

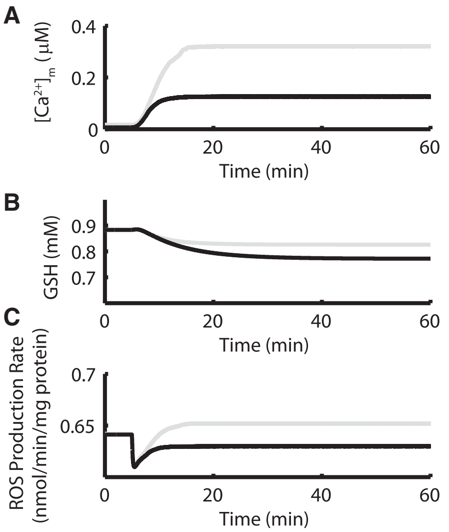

FIGURE 6 Elevated $[Na^+]_i$ limits mitochondrial Ca^{2+} uptake and depletes scavengers. (*A*) Mitochondrial Ca^{2+} accumulation is blunted in the presence of 15 mM $[Na^+]_i$ (*black*) compared to control (*gray*). (*B*) 15 mM $[Na^+]_i$ conditions (*black*) lead to increased GSH oxidation compared to control (*gray*). (*C*) Elevated cytosolic Na^+ (*black*) leads to decreased ROS production compared to control (*gray*), similar to mCU inhibition results.

Under the hypothesis that mNCE is the primary link between elevated $[Na^+]_I$ and altered mitochondrial Ca^{2+} regulation, inhibition of the mNCE is expected to restore some degree of the control of ROS emission. Simulations were performed with model $[Na^+]_I$ at 15 mM and mNCE flux reduced by 85% to simulate application of CGP37157. This decrease in mitochondrial Ca^{2+} export flux successfully counteracts the $[Na^+]_i$-dependent increase and restores $[H_2O_2]_m$ to control levels, as shown in Fig. 7 *A*. Fig. 7 *B*

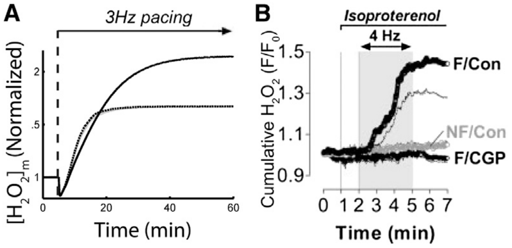

FIGURE 7 Block of mNCE with CGP reduces ROS overflow in high $[Na^+]_i$ conditions. (*A*) Model simulations using 15 mM $[Na^+]_i$ and 85% inhibition of mNCE flux to simulate CGP37157 block (*dotted line*) restore $[H_2O_2]_m$ to control levels (*gray line*). 15 mM $[Na^+]_i$ trend without CGP37157 (*black*) is shown for comparison. Simulations were started from rest with 3Hz pacing initiated at 5 min. (*B*) Experimental data in nonfailing cells (NF/Con), untreated failing cells (F/Con), and failing cells treated with CGP37157 (F/CGP) shows a similar response. Panel *B* reproduced from (15).

shows experimental data from control and HF cells with or without CGP37157 and demonstrates a similar effect.

Increased GSH pool reduces ROS overflow

Many experiments investigating the role of oxidative stress in ischemia have shown that addition of exogenous antioxidants, such as GSH, can ameliorate pathological symptoms (30,31). This mechanism was tested in the model. Fig. 8 shows that, compared to a control total matrix GSH/GSSG pool in the model of 1 mM, increasing the pool size by 25% and by 75% both result in a decrease of the ROS overflow associated with the increase in pacing frequency. Mitochondrial H_2O_2 increases by 67% after pacing compared to rest for control, 21.9% for 1.25 mM GSH pool, and 10.5% for 1.75 mM GSH pool. ROS production remains unchanged for the three protocols (not shown). The quantitative comparison of the results in Fig. 8 shows that the ROS overflow behavior of the model is very sensitive to the size of the GSH pool. Further analysis over a range of 0.5–mM GSH pool size shows that ROS overflow is the most sensitive to changes in GSH pool size near 1 mM, which is the control size in the model (Fig. 9). For pool sizes <0.9 mM, the relative increase in $[H_2O_2]_m$ appears to decrease. This effect is derived largely from the trend in resting $[H_2O_2]_m$ levels. Steady-state $[H_2O_2]_m$ at rest increases slightly with decreasing GSH pool size until the pool size drops below 0.9 mM, at which point resting $[H_2O_2]_m$ increases almost exponentially with decreasing pool size (see Fig. S5). This is indicative of GSH scavenging capacity being increasingly compromised at rest. With reduced available GSH scavenging capacity, the resting $[H_2O_2]_m$ level is already high and the increase after pacing represents a smaller relative increase. Such a comparison is difficult to quantify experimentally because GSH is usually applied to the extracellular medium, making it challenging to determine how much GSH is transported into the cytosol and the mitochondrial matrix. In the context of a computational model, many protocols are available that are not possible in an experimental setting.

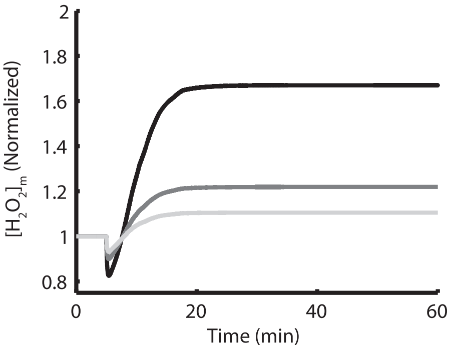

FIGURE 8 Increasing mitochondrial GSH pool size reduces the effect of increased workload in $[H_2O_2]_m$. Simulations were started from rest with 3Hz pacing initiated at 5 min. Control (1 mM pool) is black, dark gray is 25% increase in pool size, and light gray is 75% increase. ROS production for these different GSH cases is identical.

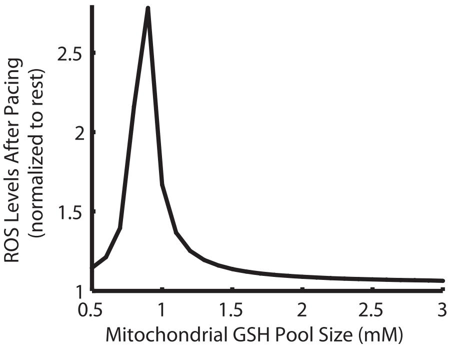

FIGURE 9 Dependence of ROS increase with pacing on mitochondrial GSH pool size. For large pools of GSH (≥ 1.9 mM) the increase in $[H_2O_2]_m$ after onset of 3Hz pacing is $<10\%$. As the mitochondrial GSH pool decreases beyond 1.9 mM, pacing-induced ROS elevation increases to a maximum of ~2.8× near 0.9 mM. For smaller pools than 0.9 mM, resting $[H_2O_2]_m$ is significantly elevated such that pacing induces a smaller increase.

DISCUSSION

In this work, we have combined a detailed model of ROS scavenging within the mitochondrial environment with a validated model of ROS production from the mitochondrial ETC. Together, the ROS production and scavenging components provide a biophysically accurate representation of the control of ROS levels in the mitochondria. This combined mitochondrial model is able to reproduce i), state 3 and state 4 steady-state energetics values and the proportion of respiratory flux diverted to ROS, ii), the proportional control of GSH and Trx systems on mitochondrial ROS emission, and iii), the magnitude and kinetics of $\Delta\Psi$ and NADH during a transition protocol from state 0 to state 4 to state 3. After these validation steps, some parameters of the model were modified (see Methods) to better simulate a mitochondrion within the cellular environment. This model is able to replicate cellular data describing i), NADH oxidation and increased H_2O_2 emission for increased workload after mCU inhibition, ii), NADH oxidation and increased H_2O_2 emission for increased workload with elevated cytosolic Na^+, iii), effective reversal of elevated $[Na^+]_i$ effects by CGP37157, and iv), decreased H_2O_2 emission for increased GSH pool size.

Model predictions

The similar fluorescence properties and disparity in size between the NAD^+/NADH and $NADP^+$/NADPH pools, with the NAD^+/NADH pool estimated to be at least 4–7× larger (32,33), lead to the measurement of an NAD(P)H signal that is more closely representative of NADH than NADPH. As such, to the authors' knowledge, the kinetics of NADPH levels in the cardiac myocyte during workload transitions have never been reported experimentally. The model presented here offers predictions of NADPH during such a protocol. These predictions are based on the use of in vitro parameters from the experimental data to constrain the rate of conversion of NADH to NADPH by THD and the validation of NADH transients against experimental data (see Fig. 2). The model predicts that although NADPH may be more reduced than NADH at rest, as NADH levels drop for the mCU inhibition and elevated $[Na^+]_i$ protocols, NADPH becomes more oxidized than NADH and the GSH and Trx scavenging systems become compromised. The proton motive force (PMF)-dependence and reversibility of the THD are key to this behavior; in well-energized mitochondria with ample TCA cycle capacity, the THD serves to bolster the antioxidant defenses, but the same enzyme can contribute to depletion of the NADPH pool when the rate of NADH oxidation exceeds its production. Given that model pH is held constant, PMF drops upon the increase in workload associated with the onset of pacing. The forward, NADPH-producing reaction of the THD is driven by the free energy of the transfer of protons in the direction of the PMF. As PMF decreases, the rate of the forward reaction decreases. At the same time, the decrease in mitochondrial Ca^{2+} drives an oxidation of NADH. The model predicts that, although IDH and αKGDH both serve as Ca^{2+}-sensitive NADH reductases, αKGDH plays a larger part in NADH control. A 10% decrease in the rate of αKGDH causes a further 3% oxidation in NADH after the onset of pacing in the uniporter block protocol, whereas a 10% decrease in IDH activity does not cause a significant change in NADH levels (not shown). The combined effects of NADH oxidation and decrease in PMF lead to a reversal of the THD and decrease in NADPH levels, which ultimately drives the ROS overflow behavior.

Although GSH/GSSG redox potential can be measured experimentally, the concentrations of GSSG and GSH are more important in analyzing the enzyme kinetics of the scavenging reactions. These concentrations are difficult to ascertain from the redox potential without a precise measurement of the size of the GSH pool, which has been estimated to vary significantly across different energetic conditions, including starvation and oxidative stress (34). The model predicts that depletion of NADPH associated with the oxidation of NADH causes an oxidation of GSH from 0.88 mM at rest to 0.83 mM for control, 0.74 mM for 90% mCU block, and 0.77 mM for high $[Na^+]_i$ during the workload transition, which results in increased H_2O_2 emission for all protocols. Given the increasing adoption of redox-sensing GFP probes (35,36), quantitative assessment of GSH and GSSG levels in vivo should be possible in the near future. A parametric study of total mitochondrial GSH pool size in the model shows that the amount of increase in H_2O_2 after onset of pacing is very sensitive to the total amount of GSH and GSSG available for pools near 1 mM. Gilbert (34) cites ~2.4 mM GSH pool in the cytoplasm of rat heart cells and asserts that cytosolic and matrix concentrations are approximately equal, based on the amount of GSH localized to the matrix of rat liver mitochondria and the volumetric ratio of the cytoplasm and mitochondrial matrix. This is in good agreement with the measurement of 2.7 mM total cytoplasmic GSH by Aon et al. (37). However, direct measurement of matrix GSH in guinea pig heart cells by Stanley et al. (38) gives a value between 1 and 1.5 mM total GSH. The model, which uses a value of 1 mM, is in good agreement with the model.

The Trx and GSH scavenger pathways both make a major contribution to cardiac mitochondrial ROS scavenging, and their individual contributions vary to some extent with species (16). Deficiencies in one pathway can be partially compensated by the other pathway, but both depend on NADPH supply. The present model not only allows one to examine the independent behaviors of the two scavenger pathways, but is the first, to our knowledge, to describe how both are coupled to the pyridine nucleotide redox potential, the proton motive force, and mitochondrial oxidative phosphorylation. Moreover, in addition to ROS scavenging, the complex effects of these factors on ROS production are taken into account by model. With respect to relative contributions of Trx and GSH to ROS scavenging rates, Fig. 3 *B* and Fig. S3 show the effects of pacing on the mitochondrial scavenging systems of control cells and those with the mCU inhibited. Both GSH and Trx show an approximate 15 mV oxidation of their redox potentials for the mCU inhibition case due to the dependence of both GR and TrxR on NADPH. However, throughout these two protocols, E_{Trx} remains more negative than E_{GSH}, reflecting a greater reducing potential for Trx compared to GSH, as initially suggested by the work of Aon et al. (16). Although some scavenging parameters differ between the mitochondrial and cellular models presented here, the results of scavenging inhibition for the mitochondrial model (Fig. S1) also support the greater role of Trx. Aon et al. (16) used auranofin and dinitrochlorobenzene to progressively inhibit the Trx and GSH systems, respectively, in isolated mitochondria, but more work will need to be carried out in myocytes to examine the contribution of each scavenger pathway to global ROS accumulation in the cell. Nonmitochondrial sources of ROS must also be taken into consideration in future models.

Perhaps the most significant prediction arising from the model results regards the changes in ROS production after workload transition. Although a naive interpretation of the increase in ROS after pacing for Ru360-incubated cells might attribute it to an increase in ROS production, the model results show that the increase in ROS levels occurs by a decrease in ROS production and an even larger decrease in ROS scavenging (Figs. 3 and 4). Future experimental studies in antioxidant-depleted cells could help validate this prediction.

Cellular control of ROS production

From experimental data, it is evident that ROS emission levels from cardiac myocytes increase after an increase in workload, but separating the role of ROS production from the role of ROS scavenging presents a challenge. We expect that ROS scavenging is compromised to some extent by the oxidation of NADH. However, there is a wide array of concomitant changes to ROS production and scavenging that will produce the same overall ROS levels. The model predicts that ROS production for the 90% mCU inhibition and elevated $[Na^+]_i$ protocols will decrease after the workload transition. The decrease in ROS production is attributable to the effects of NADH oxidation and $\Delta\Psi$ depolarization that occur during ADP addition. This follows from the mechanism of ROS Production used in the Gauthier et al. (25) ETC model, which requires high mitochondrial membrane potential and a highly reduced Q pool. ROS production during pacing for mCU inhibition and high $[Na^+]_i$ protocols is lower with respect to control because of the more oxidized NADH pool for those protocols with compromised Ca^{2+} handling, which results in a more oxidized Q pool and less driving force for ROS production.

The ROS production mechanism from complex III in the ETC-ROS model depends on the accumulation of an unstable semiquinone (SQ) on the cytosolic-side quinone binding site of complex III. The concentration of this SQ builds up as the net flux through complex III's Q cycle stagnates. Under physiological conditions, this occurs due to elevated $\Delta\Psi$, reducing the rate of electron transfer through the membrane from complex III's b_L heme to its b_H heme. Both hemes become reduced, leading electrons to stagnate upstream at the cytosolic SQ. The unpaired electron from SQ seeks stability by escaping to reduce oxygen, forming superoxide, a reactive oxygen species. Since the older models of ROS production used as the basis for the ETC-ROS model were developed, new mechanisms of ROS production from complex III have been proposed (39,40). These mechanisms do not rely on a high concentration of cytosolic-side SQ and require the availability of a threshold amount of ubiquinone to accept electrons in the reverse reaction from reduced heme b_L. This version of the model corrects the legacy value of 10 mM total NAD^+/NADH pool from Magnus and Keizer (41) that was used in the original Gauthier et al. model (25) by changing it to the 1 mM value used in Wei et al. (42) 1 mM total NAD^+/NADH pool yields better control of NAD^+- and NADH-dependent TCA cycle enzymes and is in good agreement with the $\approx$0.82 mM mitochondrial $NAD^+ +$ NADH pool size measured in the heart (43). With this updated value of the total NAD^+/NADH pool size, the accumulation of cytosolic-side SQ is dramatically reduced compared to Gauthier et al. (25). However, the ROS production model used here still requires a highly reduced Q pool. It is possible that incorporation of a different mechanism might change the workload-dependence of ROS production, which is a topic for future investigation.

Previous modeling and critique of the model

The model presented here builds on the well-validated scavenging network of Kembro et al. (17), but with dynamic ROS production adapted from Gauthier et al. (25) that varies with changes in the mitochondrial energetic state. Although Gauthier et al. (25) demonstrated the interaction of their ROS production model with a minimal model of scavenging, to the authors' knowledge, the model presented here is the first to combine dynamic ROS production and scavenging, both controlled by mitochondrial $\Delta\Psi$ and redox state. It is still important to note the existence of other ROS production or scavenging models in the literature. Models by Adimora et al. (44) and Antunes et al. (45) describe dynamic ROS scavenging, but their analyses do not include scavenging in the mitochondrial matrix or endogenous H_2O_2. Detailed modeling of ROS production was performed by Selivanov et al. (20–23) and Demin et al. (18,19), but without taking into account the mitochondrial mechanisms for degradation of ROS.

Achieving quantitative agreement between the model and the experimental data is hindered by the inability to calibrate experimental fluorescence signals representing some signaling components and the inability to measure other components at all. Q pool redox state is difficult to monitor continuously, especially in a cellular preparation. The mechanism controlling ROS production changes after pacing (described previously) might be counterintuitive, but poses just one mechanism to explain the experimental observation that ROS release from the mitochondria increases in control cells as well as cells with compromised Ca^{2+} handling. The ROS production component of the cellular model is difficult to validate experimentally and would benefit from future experimental protocols in cells depleted of both matrix and cytosolic scavenging systems.

Much remains unknown about the mitochondrial environment within the cell, though it is known that compartmentation and buffering of metabolites like ATP in the extramitochondrial space differs in cellular preparations compared to isolated mitochondria (46,47). Changes in ATP, P_i, pH, and the protonmotive force will affect the other ionic species of the mitochondria (Ca^{2+}, Na^+, H^+) via the mitochondrial ion circuits involving transporters like the phosphate carrier, mNCE, and mitochondrial Na^+/H^+ exchanger. The control of the ion circuits that was well fit in the model of Wei et al. (42) (a precursor to the ME-R model) was likely to be compromised at the high pacing frequencies associated with stimulation of isolated myocytes. For this reason, in this work, pH and $[P_i]_m$ were clamped in the cellular simulations (see Methods). Additionally, it is known that some aspects of control change with respect to that of the isolated mitochondrion (48,49). As such, it is likely that other processes are still unaccounted for in the model. For example, the β-adrenergic activation employed in the experiments of Kohlhaas et al. (15) might impact complex I function and ROS production (50). Additionally, secondary ROS effects, such as redox modulation of transporters, and changes in the permeability of the inner mitochondrial membrane may play a role in the experimental results observed. However, these more minor mechanisms would not be expected to affect the overall qualitative trends of the model or experimental results.

The mitochondrial effects of acute β-adrenergic stimulation in cardiac myocytes have been historically most closely studied via changes in Ca^{2+} signaling. The relatively recent discovery of the mitochondrial A-kinase anchor protein has focused new efforts on elucidating the phosphorylation-dependent regulatory mechanisms of the mitochondria, though the effects of direct protein kinase A (PKA) phosphorylation on mitochondria are still controversial (see (51) for review). A mitochondrial isoform of PKA is anchored to the outer mitochondrial membrane, where it is activated by elevated cytosolic cAMP levels derived from the addition of isoproterenol (52). Activated PKA phosphorylates several targets involved in cell survival, steroid metabolism, and oxidative phosphorylation (52). Although signaling pathways related to the apoptotic cascade operate on the timescale of several hours (53), cAMP-dependent regulation of complex I activity (54) and complex IV activity (55) may be relevant at the timescale of the simulations performed here. Phosphorylation pathways regulated by kinases other than PKA have also been shown to regulate mitochondrial K_{ATP} channels and the voltage-dependent anion channel (56). This first study, to our knowledge, shows the qualitative relationship of increased workload and ROS overflow using on Ca^{2+}-mediated beta-adrenergic changes, but the incorporation of mitochondrial phosphorylation pathways could pose an interesting direction for future work.

The simulations presented here do not represent a comprehensive analysis of all the processes involved in HF. In addition to elevated cytosolic Na^{+}, myocytes from failing hearts also exhibit decreased Ca^{2+} load in the sarcoplasmic reticulum (57) and smaller cytosolic Ca^{2+} transients (58). Although these mechanisms were not examined here, we hypothesize that they would further contribute to reduced mitochondrial Ca^{2+} uptake and depletion of ROS scavenging systems, exacerbating the elevated $[Na^{+}]_i$ effects examined here. These additional aspects of the HF phenotype could pose interesting directions for further study.

CONCLUSION

The integration and adaptation of previously published, dynamic models of ROS production (25) and scavenging (17) provides insight into the control of ROS levels in failing myocytes. Disruption of normal Ca^{2+} handling either by application of Ru360 or by elevated $[Na^{+}]_i$, as in HF, leads to oxidation of the mitochondrial ROS scavenging systems upon increasing workload. Although the net effect is an increase in ROS levels, the model predicts that ROS production for compromised mitochondria decreases with an increase in pacing frequency. The findings based on this model confirm the hypothesis that cells with compromised mitochondrial Ca^{2+}-handling have decreased scavenging resources, leading to increased ROS emission after workload transitions. Results from the model also suggest further experimental investigation into ROS production in the whole myocyte.

SUPPORTING MATERIAL

Five figures, sixteen tables, supplemental data, and references (59–67) are available at http://www.biophysj.org/biophysj/supplemental/S0006-3495(13)01235-6.

This work was supported by National Institutes of Health grants R01HL052160 (R.L.W.), R33HL87345 (R.L.W.), and R37HL54598 (B.O'R.). L.D.G. was supported by NDSEG and NSF graduate fellowships.

REFERENCES

1. Belch, J. J., A. B. Bridges, …, M. Chopra. 1991. Oxygen free radicals and congestive heart failure. *Br. Heart J.* 65:245–248.
2. Mallat, Z., I. Philip, …, A. Tedgui. 1998. Elevated levels of 8-iso-prostaglandin F2α in pericardial fluid of patients with heart failure: a potential role for in vivo oxidant stress in ventricular dilatation and progression to heart failure. *Circulation.* 97:1536–1539.
3. McMurray, J., M. Chopra, …, H. J. Dargie. 1993. Evidence of oxidative stress in chronic heart failure in humans. *Eur. Heart J.* 14:1493–1498.
4. Ide, T., H. Tsutsui, …, A. Takeshita. 1999. Mitochondrial electron transport complex I is a potential source of oxygen free radicals in the failing myocardium. *Circ. Res.* 85:357–363.
5. Dhalla, A. K., and P. K. Singal. 1994. Antioxidant changes in hypertrophied and failing guinea pig hearts. *Am. J. Physiol.* 266:H1280–H1285.
6. Hill, M. F., and P. K. Singal. 1996. Antioxidant and oxidative stress changes during heart failure subsequent to myocardial infarction in rats. *Am. J. Pathol.* 148:291–300.
7. Hill, M. F., and P. K. Singal. 1997. Right and left myocardial antioxidant responses during heart failure subsequent to myocardial infarction. *Circulation.* 96:2414–2420.
8. Dai, D. F., L. F. Santana, …, P. S. Rabinovitch. 2009. Overexpression of catalase targeted to mitochondria attenuates murine cardiac aging. *Circulation.* 119:2789–2797.
9. Despa, S., M. A. Islam, …, D. M. Bers. 2002. Intracellular Na(+) concentration is elevated in heart failure but Na/K pump function is unchanged. *Circulation.* 105:2543–2548.
10. Murphy, E., and D. A. Eisner. 2009. Regulation of intracellular and mitochondrial sodium in health and disease. *Circ. Res.* 104:292–303.
11. Pieske, B., L. S. Maier, …, S. Houser. 2002. Rate dependence of [Na+] i and contractility in nonfailing and failing human myocardium. *Circulation.* 106:447–453.
12. Liu, T., and B. O'Rourke. 2008. Enhancing mitochondrial Ca2+ uptake in myocytes from failing hearts restores energy supply and demand matching. *Circ. Res.* 103:279–288.
13. Maack, C., S. Cortassa, …, B. O'Rourke. 2006. Elevated cytosolic Na+ decreases mitochondrial Ca2+ uptake during excitation-contraction

coupling and impairs energetic adaptation in cardiac myocytes. *Circ. Res.* 99:172–182.

14. Liu, T., D. A. Brown, and B. O'Rourke. 2010. Role of mitochondrial dysfunction in cardiac glycoside toxicity. *J. Mol. Cell. Cardiol.* 49:728–736.
15. Kohlhaas, M., T. Liu, …, C. Maack. 2010. Elevated cytosolic Na+ increases mitochondrial formation of reactive oxygen species in failing cardiac myocytes. *Circulation.* 121:1606–1613.
16. Aon, M. A., B. A. Stanley, …, S. Cortassa. 2012. Glutathione/thioredoxin systems modulate mitochondrial H2O2 emission: an experimental-computational study. *J. Gen. Physiol.* 139:479–491.
17. Kembro, J. M., M. A. Aon, …, S. Cortassa. 2013. Integrating mitochondrial energetics, redox and ROS metabolic networks: a two-compartment model. *Biophys. J.* 104:332–343.
18. Demin, O. V., I. I. Goryanin, …, H. V. Westerhoff. 2001. Kinetic modeling of energy metabolism and superoxide generation in hepatocyte mitochondria. *Mol. Biol.* 35:940–949.
19. Demin, O. V., B. N. Kholodenko, and V. P. Skulachev. 1998. A model of O2.-generation in the complex III of the electron transport chain. *Mol. Cell. Biochem.* 184:21–33.
20. Selivanov, V. A., M. Cascante, …, T. V. Votyakova. 2012. Multistationary and oscillatory modes of free radicals generation by the mitochondrial respiratory chain revealed by a bifurcation analysis. *PLOS Comput. Biol.* 8:e1002700.
21. Selivanov, V. A., T. V. Votyakova, …, M. Cascante. 2011. Reactive oxygen species production by forward and reverse electron fluxes in the mitochondrial respiratory chain. *PLOS Comput. Biol.* 7:e1001115.
22. Selivanov, V. A., T. V. Votyakova, …, M. Cascante. 2009. Bistability of mitochondrial respiration underlies paradoxical reactive oxygen species generation induced by anoxia. *PLOS Comput. Biol.* 5:e1000619.
23. Selivanov, V. A., J. A. Zeak, …, T. V. Votyakova. 2008. The role of external and matrix pH in mitochondrial reactive oxygen species generation. *J. Biol. Chem.* 283:29292–29300.
24. Jin, Q., and C. M. Bethke. 2002. Kinetics of electron transfer through the respiratory chain. *Biophys. J.* 83:1797–1808.
25. Gauthier, L. D., J. L. Greenstein, …, R. L. Winslow. 2013. A computational model of reactive oxygen species and redox balance in cardiac mitochondria. *Biophys. J.* 105:1045–1056.
26. Popova, T., M. A. Pinheiro de Carvalho, …, L. Medvedeva. 2007. Regulation of mitochondrial NADP-isocitrate dehydrogenase in rat heart during ischemia. *Mol. Cell. Biochem.* 294:97–105.
27. Sazanov, L. A., and J. B. Jackson. 1994. Proton-translocating transhydrogenase and NAD- and NADP-linked isocitrate dehydrogenases operate in a substrate cycle which contributes to fine regulation of the tricarboxylic acid cycle activity in mitochondria. *FEBS Lett.* 344:109–116.
28. Aon, M. A., S. Cortassa, and B. O'Rourke. 2010. Redox-optimized ROS balance: a unifying hypothesis. *Biochim. Biophys. Acta.* 1797:865–877.
29. Pieske, B., and S. R. Houser. 2003. [Na+]i handling in the failing human heart. *Cardiovasc. Res.* 57:874–886.
30. Kupatt, C., R. Hinkel, …, P. Boekstegers. 2004. Selective retroinfusion of GSH and cariporide attenuates myocardial ischemia-reperfusion injury in a preclinical pig model. *Cardiovasc. Res.* 61:530–537.
31. Seiler, K. S., and J. W. Starnes. 2000. Exogenous GSH protection during hypoxia-reoxygenation of the isolated rat heart: impact of hypoxia duration. *Free Radic. Res.* 32:41–55.
32. Joubert, F., H. M. Fales, …, R. S. Balaban. 2004. NADH enzyme-dependent fluorescence recovery after photobleaching (ED-FRAP): applications to enzyme and mitochondrial reaction kinetics, in vitro. *Biophys. J.* 86:629–645.
33. Livingston, B. E., R. A. Altschuld, and C. M. Hohl. 1996. Metabolic compartmentalization in neonatal swine myocytes. *Pediatr. Res.* 40:59–65.
34. Gilbert, H. F. 1990. Molecular and cellular aspects of thiol-disulfide exchange. *Adv. Enzymol. Relat. Areas Mol. Biol.* 63:69–172.
35. Dooley, C. T., T. M. Dore, …, R. Y. Tsien. 2004. Imaging dynamic redox changes in mammalian cells with green fluorescent protein indicators. *J. Biol. Chem.* 279:22284–22293.
36. Hanson, G. T., R. Aggeler, …, S. J. Remington. 2004. Investigating mitochondrial redox potential with redox-sensitive green fluorescent protein indicators. *J. Biol. Chem.* 279:13044–13053.
37. Aon, M. A., S. Cortassa, …, B. O'Rourke. 2007. Sequential opening of mitochondrial ion channels as a function of glutathione redox thiol status. *J. Biol. Chem.* 282:21889–21900.
38. Stanley, B. A., V. Sivakumaran, …, N. Paolocci. 2011. Thioredoxin reductase-2 is essential for keeping low levels of H(2)O(2) emission from isolated heart mitochondria. *J. Biol. Chem.* 286:33669–33677.
39. Dröse, S., and U. Brandt. 2008. The mechanism of mitochondrial superoxide production by the cytochrome bc1 complex. *J. Biol. Chem.* 283:21649–21654.
40. Borek, A., M. Sarewicz, and A. Osyczka. 2008. Movement of the iron-sulfur head domain of cytochrome *bc*(1) transiently opens the catalytic Q(o) site for reaction with oxygen. *Biochemistry.* 47:12365–12370.
41. Magnus, G., and J. Keizer. 1997. Minimal model of beta-cell mitochondrial Ca2+ handling. *Am. J. Physiol.* 273:C717–C733.
42. Wei, A.-C., M. A. Aon, …, S. Cortassa. 2011. Mitochondrial energetics, pH regulation, and ion dynamics: a computational-experimental approach. *Biophys. J.* 100:2894–2903.
43. Randle, P., and P. Tubbs. 1979. Carbohydrate and fatty acid metabolism. *In* Handbook of Physiology: The Cardiovascular System. Vol. 1. R. M. Berne, N. Sperelakis, and R. Geiger, editors. Am. Physiol. Soc., Bethesda, MD.805–844.
44. Adimora, N. J., D. P. Jones, and M. L. Kemp. 2010. A model of redox kinetics implicates the thiol proteome in cellular hydrogen peroxide responses. *Antioxid. Redox Signal.* 13:731–743.
45. Antunes, F., and E. Cadenas. 2000. Estimation of H2O2 gradients across biomembranes. *FEBS Lett.* 475:121–126.
46. Joubert, F., P. Mateo, …, J. A. Hoerter. 2004. CK flux or direct ATP transfer: versatility of energy transfer pathways evidenced by NMR in the perfused heart. *Mol. Cell. Biochem.* 256–257:43–58.
47. Kaasik, A., V. Veksler, …, R. Ventura-Clapier. 2001. Energetic crosstalk between organelles: architectural integration of energy production and utilization. *Circ. Res.* 89:153–159.
48. Ramzan, R., K. Staniek, …, S. Vogt. 2010. Mitochondrial respiration and membrane potential are regulated by the allosteric ATP-inhibition of cytochrome *c* oxidase. *Biochim. Biophys. Acta.* 1797:1672–1680.
49. Kadenbach, B., R. Ramzan, …, S. Vogt. 2011. The role of mitochondrial membrane potential in ischemic heart failure. *Mitochondrion.* 11:700–706.
50. De Rasmo, D., G. Gattoni, …, A. Signorile. 2011. The β-adrenoceptor agonist isoproterenol promotes the activity of respiratory chain complex I and lowers cellular reactive oxygen species in fibroblasts and heart myoblasts. *Eur. J. Pharmacol.* 652:15–22.
51. O'Rourke, B., J. E. Van Eyk, and D. B. Foster. 2011. Mitochondrial protein phosphorylation as a regulatory modality: implications for mitochondrial dysfunction in heart failure. *Congest. Heart Fail.* 17:269–282.
52. Carlucci, A., L. Lignitto, and A. Feliciello. 2008. Control of mitochondria dynamics and oxidative metabolism by cAMP, AKAPs and the proteasome. *Trends Cell Biol.* 18:604–613.
53. Suzuki, K., S. Kostin, …, J. Schaper. 2001. Time course of the apoptotic cascade and effects of caspase inhibitors in adult rat ventricular cardiomyocytes. *J. Mol. Cell. Cardiol.* 33:983–994.
54. Technikova-Dobrova, Z., A. M. Sardanelli, …, S. Papa. 2001. Cyclic adenosine monophosphate-dependent phosphorylation of mammalian mitochondrial proteins: enzyme and substrate characterization and functional role. *Biochemistry.* 40:13941–13947.
55. Bender, E., and B. Kadenbach. 2000. The allosteric ATP-inhibition of cytochrome *c* oxidase activity is reversibly switched on by cAMP-dependent phosphorylation. *FEBS Lett.* 466:130–134.

56. Horbinski, C., and C. T. Chu. 2005. Kinase signaling cascades in the mitochondrion: a matter of life or death. *Free Radic. Biol. Med.* 38:2–11.

57. Hobai, I. A., and B. O'Rourke. 2001. Decreased sarcoplasmic reticulum calcium content is responsible for defective excitation-contraction coupling in canine heart failure. *Circulation.* 103:1577–1584.

58. Davies, C. H., K. Davia, …, S. E. Harding. 1995. Reduced contraction and altered frequency response of isolated ventricular myocytes from patients with heart failure. *Circulation.* 92:2540–2549.

59. Coreassa, S., M. A. Aon, and B. O'Rourke. 2004. A mitochondrial oscillator dependent on reactive oxygen species. *Biophys. J.* 87:2060–2073.

60. Fernandes, A. P., and A. Holmgren. 2004. Glutaredoxins: glutathione-dependent redox enzymes with functions far beyond a simple thioredoxin backup system. *Antioxid. Redox Signal.* 9:63–74.

61. Holmgren, A. 1989. Thioredoxin and glutaredoxin systems. *J. Biol. Chem.* 264:13963–13966.

62. Cox, A. G., C. C. Winterbourn, and M. B. Hampton. 2010. Mitochondrial peroxiredoxin involvement in antioxidant defence and redox signalling. *Biochem. J.* 425:313–325.

63. Sztajer, H., B. Gamain, …, L. Flohe. 2001. The putative glutathione peroxidase gene of *Plasmodium falciparum* codes for a thioredoxin peroxidase. *J. Biol. Chem.* 276:7397–7403.

64. Pillay, C. S., J. H. Hofmeyr, …, J. M. Rohwer. 2009. Enzymes or redox couples? The kinetics of thioredoxin and glutaredoxin reactions in a systems biology context. *Biochem. J.* 417:269–275.

65. Eckenroth, B., K. Harris, …, R. J. Hondal. 2006. Semisynthesis and characterization of mammalian thioredoxin reductase. *Biochemistry.* 45:5158–5170.

66. Carlberg, I., and B. Mannervik. 1984. Glutathione reductase. *Methods Enzymol.* 113:484–490.

67. Zhou, L., S. Cortassa, …, B. O'Rourke. 2009. Modeling cardiac action potential shortening driven by oxidative stress-induced mitochondrial oscillations in guinea pig cardiomyocytes. *Biophys. J.* 97:1843–1852.

Supporting Material

An Integrated Mitochondrial ROS Production and Scavenging Model: Implications for Heart Failure

Laura D. Gauthier[‡], Joseph L. Greenstein[‡],

Brian O'Rourke[†], and Raimond L. Winslow[‡],

[†]Division of Cardiology, Johns Hopkins University School of Medicine, Baltimore, Maryland, USA
and [‡]Institute for Computational Medicine, Baltimore, Maryland, USA

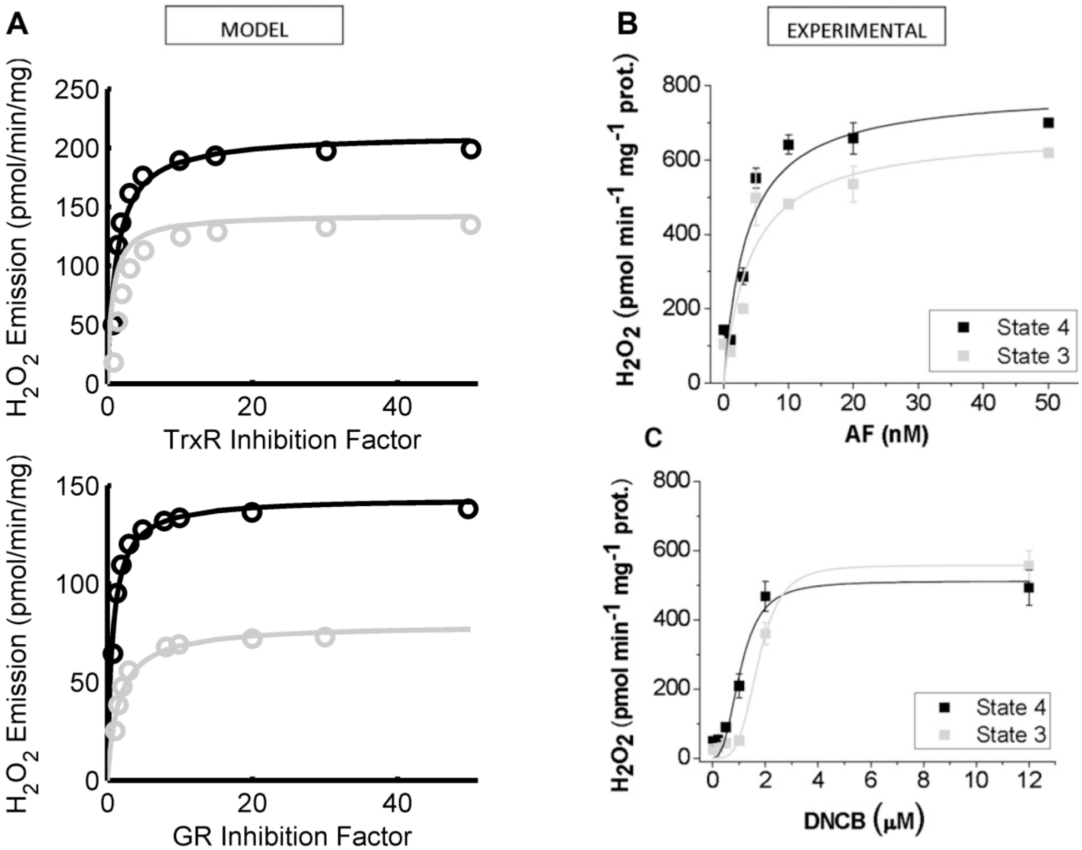

Figure S1 Steady-state mitochondrial H_2O_2 emission during inhibitory titration of GR and TrxR in state 3 and state 4. The model shows higher mitochondrial H_2O_2 emission in state 4 (black) than state 3 (blue) for both GR inhibition (A) and TrxR inhibition (B). As in the experimental data of Aon et al. (1), maximal H_2O_2 emission is greater under TrxR inhibition than under inhibition of GR.

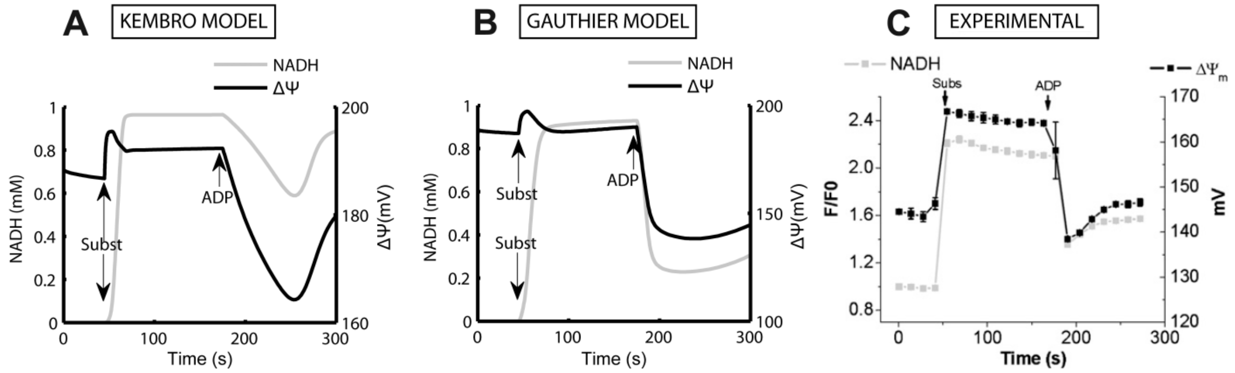

Figure S2 NADH and ΔΨ dynamics for state 0 to state 4 to state 3 transitions. (A) Kembro et al. model substrate addition (indicated by "Subst") was simulated as an increase in AcCoA and glutamate from $1x10^{-5}$ to 0.1 and $1x10^{-5}$ to 30, respectively. ADP addition represents an increase in extra-matrix ADP concentration from 0.01mM to 0.03mM, as in Kembro et al. (2), to simulate the state 4 to state 3 transition. **(B)**The same protocol for the model presented here. **(C)**Experimental data from Kembro et al. (2) show the results of the addition of 5mM G/M ("Subst") followed by 1mM ADP.

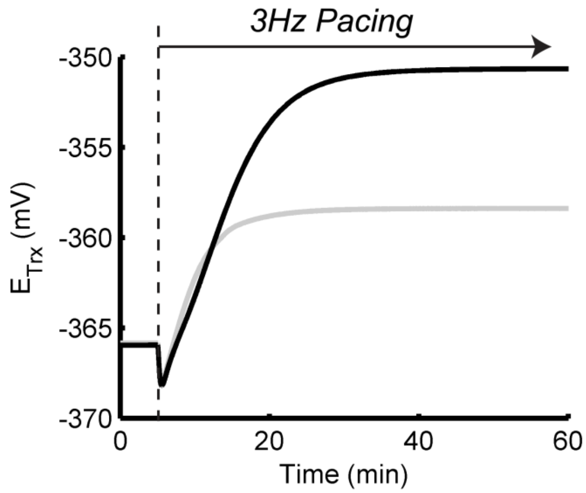

Figure S3 Thioredoxin redox potential under mCU inhibition. Decreases in NADPH also drive the oxidation of mitochondrial $Trx(SH)_2$ under control conditions (gray) and more extensively in the presence of mCU inhibition (black).

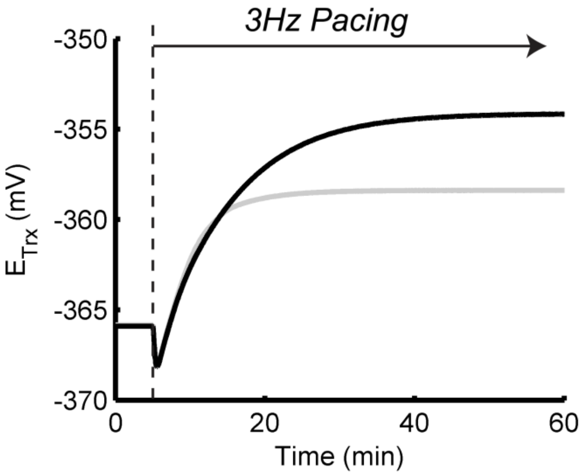

Figure S4 Elevated $[Na^+]_i$ depletes thioredoxin pool. 15mM $[Na^+]_i$ conditions (black) lead to a larger oxidation of the mitochondrial thioredoxin pool after the onset of pacing compared with control conditions (gray).

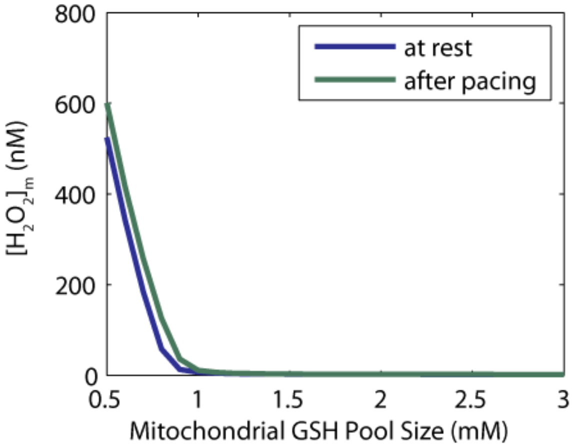

Figure S5: Decreased mitochondrial GSH pool size elevates resting $[H_2O_2]_m$. As the mitochondrial GSH pool size is decreased from 3mM to 1mM, resting $[H_2O_2]_m$ increases slightly. For decreases beyond 1mM, resting $[H_2O_2]_m$ is significantly elevated.

Notes on table 1:

Respiratory flux is given as ($VNO+VO_2SDH$) for Kembro et al. model (in units of mM O/ms) or 2*VO2 (where VO2 is actually in units of mM O_2/ms) for this model, then adjusted to match the experimental data units with a scale factor of 2*60e3 to convert from mM/ms to nmol/min/mg protein.

Mitochondrial ROS Production and Scavenging Model

Table S1 System of differential and algebraic equations used in the ME-R model

$\frac{d[Ca^{2+}]_m}{dt} = \delta_{Ca}\left(V_{uni} - V_{NaCa}\right)$	(S4)
$\frac{d\ [ADP]_m}{dt} = V_{ANT} - V_{ATPase} - V_{SL}$	(S5)
$\frac{d\Delta\Psi_m}{dt} = \frac{V_{He} + V_{He(SDH)} - V_{Hu} - V_{ANT} - V_{Hleak} - V_{NaCa} - 2V_{uni} - V_{IMAC}}{C_{mito}}$	(S6)
$\frac{d[NADH]_m}{dt} = V_{O_2} + V_{IDH} + V_{KGDH} + V_{MDH} - V_{THD}$	(S7)
$\frac{d[H^+]_m}{dt} = \delta_M\left(-V_{He} - V_{He(SDH)} + V_{Hu} + V_{NaH} + V_{PiC} + V_{Hleak}\right)$	(S8)
$\frac{d[Pi]_m}{dt} = -V_{ATPase} + V_{PiC} - V_{SL}$	(S9)
$\frac{d[ISOC]}{dt} = V_{ACO} - V_{IDH} - V_{IDH\_NADP}$	(S10)
$\frac{d[\alpha KG]}{dt} = V_{IDH} + V_{IDH\_NADP} - V_{KGDH} + V_{ATT}$	(S11)
$\frac{d[SCoA]}{dt} = V_{KGDH} - V_{SL}$	(S12)
$\frac{d[Suc]}{dt} = V_{SL} - V_{O_2SDH}$	(S13)
$\frac{d[FUM]}{dt} = V_{O_2SDH} - V_{FH}$	(S14)
$\frac{d[MAL]}{dt} = V_{FH} - V_{MDH}$	(S15)
$\frac{d[OAA]}{dt} = V_{MDH} - V_{CS} - V_{AAT}$	(S16)
$\frac{d[NADPH]_m}{dt} = V_{IDH\_NADP} + V_{THD} - V_{GRm} - V_{TxRm}$	(S17)
$\frac{d[O_2^{\cdot -}]_m}{dt} = shunt\left(V_{O_2} + V_{O_2SDH}\right) - V_{MnSOD} - V_{ROS}^{Tr}$	(S18)
$\frac{d[O_2^{\cdot -}]_i}{dt} = \frac{v_m}{v_i} V_{ROS}^{Tr} - V_{CuZnSOD}$	(S19)
$\frac{d[H_2O_2]_m}{dt} = \frac{1}{2} V_{MnSOD} - V_{difH_2O_2} - V_{GPXm} - V_{TxPXm}$	(S20)

$$\frac{d[H_2O_2]_i}{dt} = \frac{1}{2}V_{CuZnSOD} + \frac{v_m}{v_i}V_{difH_2O_2} - V_{GPXi} - V_{TxPXi} - V_{CAT} \tag{S21}$$

$$\frac{d[GSH]_m}{dt} = V_{GRm} - V_{GPXm} - V_{GRXm} + V_{GST} - V_{PSSGm} \tag{S22}$$

$$\frac{d[GSH]_i}{dt} = V_{GRi} - V_{GPXi} - V_{GRXi} + \frac{v_m}{v_i}V_{GST} - V_{PSSGi} \tag{S23}$$

$$\frac{d[GSSG]_m}{dt} = 0.5(V_{GPXm} - V_{GRm}) + V_{GRXm} \tag{S24}$$

$$\frac{d[TxR]_m}{dt} = V_{TxRm} - V_{TxPXm} \tag{S25}$$

$$\frac{d[TxR]_i}{dt} = V_{TxRi} - V_{TxPXi} \tag{S26}$$

$$\frac{d[PSSG]_m}{dt} = V_{PSSGm} - V_{GRXm} \tag{S27}$$

$$\frac{d[PSSG]_i}{dt} = V_{PSSGi} - V_{GRXi} \tag{S28}$$

Note that the differential equations for H2O2 contain corrections with regard to the stoichiometry of superoxide dismutase flux.

Computational modeling of Reactive Oxygen Species scavenging systems

The upgraded two-compartment computational model of mitochondrial energetics-redox (ME-R) includes: (i) a complete array of antioxidant defenses in two compartments: mitochondrial matrix and extra-matrix (e.g. intermembrane space, cytoplasm); and (ii) two of the three main NADPH providers in mitochondria: NADP$^+$-dependent isocitrate dehydrogenase (IDH2) in the TCA cycle, and transhydrogenase (THD). In this section we will provide a detailed description of the antioxidant defenses and mitochondrial NADPH handling.

Modeling superoxide dismutase

$$\mathrm{V_{MnSOD}} = \frac{2\,\mathrm{k^1_{SOD}}\,\mathrm{k^5_{SOD}}\left(\mathrm{k^1_{SOD}} + \mathrm{k^3_{SOD}}\left(1 + \frac{[\mathrm{H_2O_2}]\mathrm{m}}{\mathrm{K_i^{H_2O_2}}}\right)\right)\mathrm{E^T_{MnSOD}}\ [\mathrm{O_2^{\cdot -}}]\mathrm{m}}{\mathrm{k^5_{SOD}}\left(2\,\mathrm{k^1_{SOD}} + \mathrm{k^3_{SOD}}\left(1 + \frac{[\mathrm{H_2O_2}]\mathrm{m}}{\mathrm{K_i^{H_2O_2}}}\right)\right) + [\mathrm{O_2^{\cdot -}}]\mathrm{m}\ \mathrm{k^1_{SOD}}\,\mathrm{k^3_{SOD}}\left(1 + \frac{[\mathrm{H_2O_2}]\mathrm{m}}{\mathrm{K_i^{H_2O_2}}}\right)} \tag{S29}$$

$$\mathrm{V_{CuZnSOD}} = \frac{2\,\mathrm{k^1_{SOD}}\,\mathrm{k^5_{SOD}}\left(\mathrm{k^1_{SOD}} + \mathrm{k^3_{SOD}}\left(1 + \frac{[\mathrm{H_2O_2}]_\mathrm{i}}{\mathrm{K_i^{H_2O_2}}}\right)\right)\mathrm{E^T_{CuZnSOD}}\ [\mathrm{O_2^{\cdot -}}]_i}{\mathrm{k^5_{SOD}}\left(2\,\mathrm{k^1_{SOD}} + \mathrm{k^3_{SOD}}\left(1 + \frac{[\mathrm{H_2O_2}]_\mathrm{i}}{\mathrm{K_i^{H_2O_2}}}\right)\right) + [\mathrm{O_2^{\cdot -}}]_i\ \mathrm{k^1_{SOD}}\,\mathrm{k^3_{SOD}}\left(1 + \frac{[\mathrm{H_2O_2}]_i}{\mathrm{K_i^{H_2O_2}}}\right)} \tag{S30}$$

H_2O_2 transport

H_2O_2 can diffuse freely between the two compartments, following the equation:

$$V_{diff_{H_2O_2}} = c_{diff_{H_2O_2}}([H_2O_2]_m - [H_2O_2]_i) \tag{S31}$$

Gluthathione and glutaredoxin systems

The gluthathione system was present in both mitochondrial matrix and extra-matrix compartments and expressed as a system of equations comprising glutathione peroxidase (V_{GPx}) and reductase (V_{GR}) activities. The rate expressions for V_{GPx} and V_{GR} used in the model were formulated as described in our mitochondrial model of ROS metabolism (3).

$$V_{GPX_m} = \frac{E_T^{GPXm}[\mathrm{H_2O_2}]_\mathrm{m}\,[\mathrm{GSH}]_\mathrm{m}}{\Phi_1[\mathrm{GSH}]_\mathrm{m} + \Phi_2[\mathrm{H_2O_2}]_\mathrm{m}} \tag{S32}$$

$$V_{GPX_i} = \frac{E_T^{GPXi}[\mathrm{H_2O_2}]_\mathrm{i}\,[\mathrm{GSH}]_\mathrm{i}}{\Phi_1[\mathrm{GSH}]_\mathrm{i} + \Phi_2[\mathrm{H_2O_2}]_\mathrm{i}} \tag{S33}$$

$$V_{GR_m} = \frac{\mathrm{k_{GR}^1}\ \mathrm{E_T^{GRm}}}{1+\frac{\mathrm{K_M^{GSSG}}}{[\mathrm{GSSG}]}+\frac{\mathrm{K_M^{NADPH}}}{[\mathrm{NADPH}]_\mathrm{m}}+\frac{\mathrm{K_M^{GSSG}}\quad\mathrm{K_M^{NADPH}}}{[GSSG]_m[\mathrm{NADPH}]_\mathrm{m}}} \tag{S34}$$

$$V_{GR_i} = \frac{\mathrm{k_{GR}^1}\ \mathrm{E_T^{GRi}}}{1+\frac{\mathrm{K_M^{GSSG}}}{\mathrm{V}_{GSS}}+\frac{\mathrm{K_M^{NADPH}}}{[\mathrm{NADPH}]_\mathrm{i}}+\frac{\mathrm{K_M^{GSSG}}\quad\mathrm{K_M^{NADPH}}}{[GSSG]_i[\mathrm{NADPH}]_\mathrm{i}}} \tag{S35}$$

The glutaredoxin system can then detoxify the glutathionylated proteins and uses GSH as cofactor (4, 5).

$$V_{GRX_m} = \frac{k_{grx_m}\ K_{eq}^{GRX}\,([GSH]_m)^2\ \ GrxT\ \ [PSSG]_m}{([\mathrm{GSSG}]_\mathrm{m}+K_{eq}^{GRX}\,([GSH]_m)^2)\left(\frac{K_{eq}^{GRX}\,([GSH]_m)^2\ GrxT}{[\mathrm{GSSG}]_\mathrm{m}+K_{eq}^{GRX}\,([GSH]_m)^2}+K_m^{Grx}\right)([\mathrm{PSSG}]_\mathrm{m}+K_m^{PSSG})} \tag{S36}$$

$$V_{GRX_i} = \frac{k_{grx_i}\,K_{eq}^{GRX}\,([GSH]_i)^2\ \ GrxT\ \ [PSSG]_i}{(\mathrm{V_{GSS}}+K_{eq}^{GRX}\,([GSH]_i)^2)\left(\frac{K_{eq}^{GRX}\,([GSH]_i)^2\ GrxT}{[GSSG]_i+K_{eq}^{GRX}\,([GSH]_i)^2}+K_m^{Grx}\right)([\mathrm{PSSG}]_\mathrm{i}+K_m^{PSSG})} \tag{S37}$$

$$V_{PSSG_m} = \frac{k_{PSH}^1\ E_T^{PSH}\,(PSSGT-[PSSG]_m)}{\left(1+\frac{K_M^{GSH}}{[GSH]_m}\right)\left(1+\frac{[H_2O_2]m}{K_{act}^{H2O2}}\right)} \tag{S38}$$

$$V_{PSSG_i} = \frac{k_{PSH}^1\ E_T^{PSH}\,(PSSGT-[PSSG]_i)}{\left(1+\frac{K_M^{GSH}}{[GSH]_i}\right)\left(1+\frac{[H_2O_2]_i}{K_{act}^{H2O2}}\right)} \tag{S39}$$

We have assumed that the total pool of glutathione, G_T, is conserved, as indicated by equation S40, and from there the GSSG concentration in the extra-matrix compartment can be estimated (Eq. S41).

$$\mathrm{G}_T = \mathrm{G}_T - [\mathrm{GSH}]_\mathrm{m} - [\mathrm{GSH}]_i - 2\,[\mathrm{GSSG}] - [\mathrm{PSSG}]_\mathrm{m} - [\mathrm{PSSG}]_\mathrm{i} - 2\,[GSSG]_i \tag{S40}$$

$$[\mathrm{GSSG}]_i = 0.5\,(\mathrm{G}_T - [\mathrm{GSH}]_\mathrm{m} - [\mathrm{GSH}]_i - 2\,[\mathrm{GSSG}]_\mathrm{m} - [\mathrm{PSSG}]_\mathrm{m} - [\mathrm{PSSG}]_\mathrm{i}) \tag{S41}$$

In addition we have included passive GSH transport (V_{GST}) across the inner mitochondrial membrane.

$$V_{GST} = c_{GST}\,\frac{([GSH]_i - [GSH]_m)}{[GSH]_i + k_{0.5}^{GST}} \tag{S42}$$

Thioredoxin system

The Trx system includes peroxiredoxin (V_{Prx3}) and thioredoxin reductase (V_{TrxR}) (6). The rate expression for V_{TPrx3} was derived on the basis of the experimental studies performed by (7), from which we also obtained the rate constants. V_{TrxR} represents a Michaelis-Menten rate expression with two substrates (NADPH and Trx(SS) with kinetic parameters derived from refs. (8) and (9).

$$V_{Prx3_m} = \frac{E_T^{Prx3m}[H_2O_2]_m\,[TrxSH_2]_m}{\Phi_{1Prx}[TrxSH_2]_m + \Phi_{2Prx}[H_2O_2]_m} \tag{S43}$$

$$V_{Prx_i} = \frac{E_T^{Prxi}[\mathrm{H_2O_2}]_\mathrm{i}\,[\mathrm{TrxSH_2}]_\mathrm{i}}{\Phi_{1Prx}[\mathrm{TrxSH_2}]_\mathrm{i} + \Phi_{2Prx}[\mathrm{H_2O_2}]_i} \tag{S44}$$

$$V_{TrxR_m} = \frac{k_{TrxR}^1\;E_T^{TrxR2m}}{1 + \frac{K_M^{TrxSS}}{[TrxSS]_m} + \frac{K_{Mtrx}^{NADPH}}{[NADPH]_m} + \frac{K_M^{TrxSS}\quad K_{Mtrx}^{NADPH}}{[TrxSS]_m[NADPH]_m}} \tag{S45}$$

$$V_{TrxR_i} = \frac{k_{TrxR}^1\;E_T^{TrxRi}}{1 + \frac{K_M^{TrxSS}}{[TrxSS]_i} + \frac{K_{Mtrx}^{NADPH}}{[NADPH]_i} + \frac{K_M^{TrxSS}\quad K_{Mtrx}^{NADPH}}{[TrxSS]_i[NADPH]_i}} \tag{S46}$$

$$[\mathrm{TrxSS}]_\mathrm{m} = TrxT_m - [\mathrm{TrxSH_2}]_\mathrm{m} \tag{S47}$$

$$[\mathrm{TrxSS}]_\mathrm{i} = TrxT_i - [\mathrm{TrxSH_2}]_\mathrm{i} \tag{S48}$$

Extra-matrix Catalase

$$V_{CAT} = 2k_{CAT}^1 E_{CAT}^T [\mathrm{H_2O_2}]_\mathrm{i}\, e^{-fr[\mathrm{H_2O_2}]_\mathrm{i}}$$

Scavenging parameters are the same as in Kembro et al. with the exception of enzyme concentrations for GR and Trx, which were adjusted to match the proportional control of scavenging demonstrated in Figure 4.2.

Table S2 Parameter values used in the simulations: ROS production and scavenging – mitochondrial model

Symbol	Value	Units	Description	Eq	Reference
$\mathrm{k}_{\mathrm{SOD}}^{1}$	1.2×10^{3}	$\mathrm{mM}^{-1}\mathrm{ms}^{-1}$	Second-order rate constant of SOD	S29,S30	(2)
$\mathrm{k}_{\mathrm{SOD}}^{3}$	24	$\mathrm{mM}^{-1}\mathrm{ms}^{-1}$	Second-order rate constant of SOD	S29,S30	(2)
$\mathrm{k}_{\mathrm{SOD}}^{5}$	2.4×10^{-4}	ms^{-1}	First-order rate constant of SOD	S29,S30	(2)
$\mathrm{K}_{\mathrm{i}}^{\mathrm{H_2O_2}}$	0.5	mM	Inhibition constant for H_2O_2	S29,S30	(2)
$\mathrm{E}_{\mathrm{MnSOD}}^{\mathrm{T}}$	3×10^{-4}	mM	Mitochondrial matrix concentration of MnSOD	S29	(2)
$\mathrm{E}_{\mathrm{CuZnSOD}}^{\mathrm{T}}$	2.4×10^{-4}	mM	Concentration of Cu,ZnSOD	S30	(2)
$c_{diff_{H_2O_2}}$	2×10^{-4}	ms^{-1}	Diffusion constant for H_2O_2	S31	(2)
Φ_1	5.0×10^{-3}	mM ms	Constant for GPX activity	S32,S33	(2)
Φ_2	0.75	mM ms	Constant for GPX activity	S32,S33	(2)
E_T^{GPXm}	1×10^{-4}	mM	Mitochondrial matrix concentration of GPX	S32	(2)
E_T^{GPXi}	5×10^{-5}	mM	Extra-matrix concentration of GPX	S33	(2)
$\mathrm{k}_{\mathrm{GR}}^{1}$	2.5×10^{-3}	ms^{-1}	Catalytic constant of GR	S34,S35	(2)
$\mathrm{E}_{\mathrm{T}}^{\mathrm{GRm}}$	2.25×10^{-4}	mM	Mitochondrial matrix concentration of GR	S34	Adjusted
$\mathrm{E}_{\mathrm{T}}^{\mathrm{GRi}}$	2.25×10^{-4}	mM	Extra-matrix concentration of GR	S35	Adjusted
$\mathrm{K}_{\mathrm{M}}^{\mathrm{NADPH}}$	0.015	mM	Michaelis constant for NADPH of GR	S34,S35	(2)
$\mathrm{K}_{\mathrm{M}}^{\mathrm{GSSG}}$	0.06	mM	Michaelis constant for GSSG of GR	S34,S35	(2)
$[\mathrm{NADPH}]_{\mathrm{i}}$	7.5×10^{-2}	mM	Extra-matrix NADPH concentration	S34,S35	(2)
G_{T}	6	mM	Total pool of glutathione	S40,S41	(2)
k_{grx_m}	3.6×10^{-4}	$\mathrm{mM\ s}^{-1}$	Rate constant of mitochondrial matrix glutaredoxin reaction	S36	(2)
k_{grx_i}	3.6×10^{-4}	$\mathrm{mM\ s}^{-1}$	Rate constant of extra-matrix glutaredoxin reaction	S37	(2)

K_{eq}^{GRX}	1.37×10^{-3}	mM^{-1}	Equilibrium constant of glutaredoxin	S36,S37	(2)
K_{m}^{Grx}	0.01	mM	Michaelis constant for GSH of GRX	S36,S37	(2)
K_{m}^{PSSG}	0.0005	mM	Michaelis constant for glutathionylated protein of glutaredoxin	S36,S37	(2)
k_{PSH}^{1}	0.64	ms^{-1}	Rate constant of protein glutathionylation	S38,S39	(2)
E_{T}^{PSH}	8×10^{-4}	mM	Concentration of proteins that can become glutathionylated	S38,S39	(2)
K_{M}^{GSH}	0.75	mM	Michaelis constant of GSH for glutathionylation	S38,S39	(2)
K_{act}^{H2O2}	1×10^{-3}	mM	Activation constant of H_2O_2 for protein glutathionylation	S38,S39	(2)
$GrxT$	0.002	mM	Glutaredoxin concentration	S38,S39	(2)
c_{GST}	1.5×10^{-8}	ms^{-1}	Rate constant of glutathione transporter	S42	(2)
$k_{0.5}^{GST}$	2.6	mM	transport association constant of GSH	S42	(2)
E_{T}^{Prx3m}	3.0×10^{-3}	mM	Mitochondrial matrix concentration of Trx peroxidase (Prx)	S43	(2)
E_{T}^{Prx3i}	0.1	mM	Extra-matrix concentration Prx	S44	(2)
Φ_{1Prx}	3.83	mM ms	Constant for TxPX activity	S43,S44	(2)
Φ_{2Prx}	1.85	mM ms	Constant for TxPX activity	S43,S44	(2)
$\mathrm{E_{T}^{TrxR2m}}$	1.225×10^{-4}	mM	Mitochondrial matrix concentration of TrxR2	S45	Adjusted
$\mathrm{E_{T}^{TrxRi}}$	1.225×10^{-4}	mM	Extra-matrix concentration of TrxR	S46	Adjusted
$\mathrm{K_{M}^{TrxSS}}$	0.035	mM	Michaelis constant for oxidized Trx [Trx[SS]] of TrxR	S45,S46	(2)
$\mathrm{K_{M,\,Trx}^{NADPH}}$	0.012	mM	Michaelis constant for NADPH of TrxR	S45,S46	(2)
k_{TrxR}^{1}	22.75×10^{-3}	ms^{-1}	Rate constant of TrxR	S45,S46	(2)
$TrxT_{m}$	0.025	mM	Total pool of mitochondrial matrix thioredoxin	S47	(2)
$TrxT_{i}$	0.05	mM	Total pool of extra-matrix thioredoxin	S48	(2)

k_{CAT}^{1}	17	$mM^{-1}ms^{-1}$	Rate constant of catalase (CAT)	S49	(2)
E_{CAT}^{T}	1.0×10^{-6}	mM	Extra-matrix concentration of CAT	S49	(2)
fr	5.0×10^{-2}	mM^{-1}	Hydrogen peroxide inhibition factor of CAT	S49	(2)

Adjustments were made to several of the scavenging parameters for the cellular model to better approximate the experimental results for isolated myocytes undergoing high frequency pacing. Parameters not included in **Table S3** remain the same as those specified in **Table S2**.

Table S3 Parameter values used in the simulations: ROS production and scavenging – cellular model

Symbol	Value	Units	Description	Eq	Reference
Φ_1	5.0×10^{-5}	mM ms	Constant for GPX activity	S32,S33	Adjusted
Φ_2	27	mM ms	Constant for GPX activity	S32,S33	Adjusted
E_T^{GPXm}	9.77×10^{-5}	mM	Mitochondrial matrix concentration of GPX	S32	Adjusted
$\mathrm{E_T^{GRm}}$	2.3×10^{-3}	mM	Mitochondrial matrix concentration of GR	S34	Adjusted
$\mathrm{K_M^{NADPH}}$	6.54×10^{-2}	mM	Michaelis constant for NADPH of mitochondrial GR	S34,S35	Adjusted
$\mathrm{K_M^{GSSG}}$	20.6×10^{-3}	mM	Michaelis constant for GSSG of mitochondrial GR	S34,S35	(10)
$\mathrm{G_{T,mito}}$	1	mM	Total mitochondrial pool of glutathione	S40,S41	Adjusted
$\mathrm{G_{T,cyto}}$	2	mM	Total cytosolic pool of glutathione	S40,S41	(11)
E_T^{PSH}	0	mM	Concentration of proteins that can become glutathionylated	S38,S39	
$GrxT$	0	mM	Glutaredoxin concentration	S38,S39	
c_{GST}	0	ms^{-1}	Rate constant of glutathione transporter	S42	
$\mathrm{E_T^{TrxR2m}}$	3.5×10^{-4}	mM	Mitochondrial matrix concentration of TrxR2	S45	(2)
$\mathrm{E_T^{TrxRi}}$	3.5×10^{-4}	mM	Extra-matrix concentration of TrxR	S46	(2)
$\mathrm{K_{M,\,Trx}^{NADPH}}$	0.065	mM	Michaelis constant for NADPH of TrxR	S45,S46	Adjusted

Mitochondrial NADPH handling – mitochondrial model

In this section we will provide a detailed description of the mitochondrial NADPH handling.

$$NADPm = C_{NADPm} - [NADPH]_m \tag{S50}$$

$$V_{IDP\_NADP} = \left(1 + \frac{[H^{+}]_{m}}{k_{m\_IDP}^{H+}}\right)\left(1 + \frac{[ISOC]}{k_{m\_IDP}^{ISOC}} + \frac{NADP_{m}}{k_{m\_IDP}^{NADP}}\left(1 + \frac{k_{i\_IDP}^{NADP}}{NADP_{m}}\right) + \frac{[aKG]}{k_{m\_IDP}^{aKG}} + \frac{[NADPH_{m}]}{k_{m\_IDP}^{NADPH}} + \frac{[ISOC]}{k_{m\_IDP}^{ISOC}}\,\frac{NADP_{m}}{k_{m\_IDP}^{NADP}}\left(1 + \frac{k_{i\_IDP}^{NADP}}{NADP_{m}}\right) + \frac{[aKG]}{k_{m\_IDP}^{aKG}}\,\frac{[NADPH_{m}]}{k_{m\_IDP}^{NADPH}} + \frac{[ISOC]}{k_{m\_IDP}^{ISOC}}\,\frac{[NADPH_{m}]}{k_{m\_IDP}^{NADPH}} + \frac{[aKG]}{k_{m\_IDP}^{aKG}}\,\frac{NADP_{m}}{k_{m\_IDP}^{NADP}}\left(1 + \frac{k_{i\_IDP}^{NADP}}{NADP_{m}}\right)\right) \qquad \text{(S51)}$$

$$V_{IDH_{NADP}} = \frac{V_{f}^{IDH}\frac{k[ISOC]NADP_{m}}{k_{m\_IDP}^{ISOC}k_{m\_IDP}^{NADP}}\left(1+\frac{k_{i\_IDP}^{NADP}}{VNADH_{m}}\right) - V_{b}^{IDH}\frac{[aKG]\;[NADP_{m}]}{k_{m\_IDP}^{aKG}k_{m\_IDP}^{NADPH}}}{V_{IDP\_NADP}} \qquad \text{(S52)}$$

$$V_{THDen} =$$
$$1 + \frac{[NADH_{m}]}{k_{m\_THD}^{NADHm}} + \frac{NAD}{k_{m\_THD}^{NAD}} + \frac{NADP_{m}}{k_{m\_THD}^{NADP}} + \frac{[NADPH_{m}]}{k_{m\_THD}^{NADPH}} + \frac{[NADH_{m}]}{k_{m\_THD}^{NADHm}}\frac{NADP_{m}}{k_{m\_THD}^{NADP}}e^{(F/10RT).\Delta\mu_{H}} + \frac{[NADPH_{m}]}{k_{m\_THD}^{NADPH}}\frac{[NADH_{m}]}{k_{m\_THD}^{NADHm}}\,e^{(1-(F/10RT).\Delta\mu_{H})} + \frac{NAD}{k_{m\_THD}^{NAD}}\frac{NADP_{m}}{k_{m\_THD}^{NADP}}e^{(F/10RT)\Delta\mu_{H}}.\,e^{(1-(F/10RT).\Delta\mu_{H})} + \frac{[NADH_{m}]}{k_{m\_THD}^{NADHm}}\frac{[NADPH_{m}]}{k_{m\_THD}^{NADPH}} \qquad \text{(S53)}$$

$$V_{THD} = \frac{E_{T}^{THD}.k_{a}^{THD}\,\frac{[NADH]mNADP_{m}}{k_{m\_THD}^{NADHm}\;k_{m\_THD}^{NADP}}e^{(F/10RT).\Delta\mu_{H}} - E_{T}^{THD}.k_{b}^{THD}\frac{NAD\;\;[NADPH_{m}]}{k_{m\_THD}^{NAD}\;k_{m\_THD}^{NADPH}}\,e^{\left(1-(F/10RT).\Delta\mu_{H}\right)}}{V_{THDen}} \qquad \text{(S54)}$$

Table S4 Parameter values used in the simulations: Mitochondrial NADPH handling – mitochondrial model

Symbol	Value	Units	Description	Eq.	Reference
C_{NADPm}	0.1	mM	Sum of NADPH plus NADP^{+}	S50	(2)
$k_{m\_IDP}^{H+}$	0.5	mM	Dissociation constant for H^{+} of IDH2	S51	(2)
$k_{m\_IDP}^{ISOC}$	3.9×10^{-3}	mM	Michaelis constant for ISOC in IDH2	S51,S52	(2)
$k_{m\_IDP}^{NADP}$	6.7×10^{-3}	mM	Michaelis constant for NADP in IDH2	S51,S52	(2)
$k_{i\_IDP}^{NADP}$	2×10^{-6}	mM	Inhibition constant for NADP in IDH2	S51,S52	(2)
$k_{m\_IDP}^{NADPH}$	1.2×10^{-2}	mM	Michaelis constant for NADPH in IDH2	S51,S52	(2)
$k_{m\_IDP}^{aKG}$	0.51	mM	Michaelis constant for αKG in IDH2	S51,S52	(2)
V_{f}^{IDH}	8.72×10-5	mM ms^{-1}	Maximal rate of IDH2 in the forward direction	S52	(2)
V_{b}^{IDH}	5.45×10^{-6}	mM ms^{-1}	Maximal rate of IDH2 in the reverse direction	S52	(2)
$k_{m\_THD}^{NADPH}$	0.02	mM	Michaelis constant for NADPH in transhydrogenase (THD)	S53,S54	(2)
$k_{m\_THD}^{NADHm}$	0.01	mM	Michaelis constantfor NADH in THD	S53,S54	(2)
$k_{m\_THD}^{NAD}$	0.125	mM	Michaelis constant for NAD in THD	S53,S54	(2)
$k_{m\_THD}^{NADP}$	0.017	mM	Michaelis constant for NADP in THD	S53,S54	(2)

E_T^{THD}	1.1875×10^{-5}	mM	Concentration of THD enzyme	S54	(2)
k_f^{THD}	1.17474	ms^{-1}	Forward catalytic constant of THD	S54	(2)
k_b^{THD}	10	ms^{-1}	Reverse catalytic constant of THD	S54	(2)

Mitochondrial NADPH handling – cellular model

In this section we will provide a detailed description of the mitochondrial NADPH handling.

$$V_{THD} = \frac{E_T^{THD}.k_a^{THD}\frac{[NADH]m\,NADPm}{k_{m\_THD}^{NADHm}\;k_{m\_THD}^{NADP}}e^{(xdF/RT).\Delta\mu_H} - E_T^{THD}.k_b^{THD}\frac{NAD\;\;[NADPH_m]}{k_{m\_THD}^{NAD}\;k_{m\_THD}^{NADPH}}\,e^{\left(x(d-1)F/RT).\Delta\mu_H\right)}}{V_{THDen}} \qquad \text{(S54)}$$

Table S5 Parameter values used in the simulations: Mitochondrial NADPH handling – cellular model

Symbol	Value	Units	Description	Eq.	Reference
$k_{m\_IDP}^{ISOC}$	0.045	mM	Michaelis constant for ISOC in IDH2	S51,S52	(12)
$k_{m\_IDP}^{NADP}$	0.046	mM	Michaelis constant for NADP in IDH2	S51,S52	(12)
$k_{i\_IDP}^{NADP}$	2×10^{-6}	mM	Inhibition constant for NADP in IDH2	S51,S52	(2)
$k_{m\_IDP}^{NADPH}$	1.2×10^{-2}	mM	Michaelis constant for NADPH in IDH2	S51,S52	(2)
$k_{m\_IDP}^{\alpha KG}$	0.080	mM	Michaelis constant for αKG in IDH2	S51,S52	(12)
V_f^{IDH}	8.72×10^{-2}	mM ms^{-1}	Maximal rate of IDH2 in the forward direction	S52	Adjusted
V_{fb}^{IDH}	5.45×10^{-3}	mM ms^{-1}	Maximal rate of IDH2 in the reverse direction	S52	Adjusted
$k_{m\_THD}^{NADPH}$	4×10^{-3}	mM	Michaelis constant for NADPH in transhydrogenase (THD)	S53,S54	Adjusted
$k_{m\_THD}^{NADHm}$	0.01	mM	Michaelis constant for NADH in THD	S53,S54	(2)
$k_{m\_THD}^{NAD}$	0.125	mM	Michaelis constant for NAD in THD	S53,S54	(2)
$k_{m\_THD}^{NADP}$	0.02	mM	Michaelis constant for NADP in THD	S53,S54	Adjusted
E_T^{THD}	1×10^{-3}	mM	Concentration of THD enzyme	S54	Adjusted
k_f^{THD}	1.17474	ms^{-1}	Forward catalytic constant of THD	S54	(2)
k_b^{THD}	17.2756	ms^{-1}	Reverse catalytic constant of THD	S54	Adjusted

d	0.5	(13)
x	0.1	(13)

Mitochondrial Model of Energy Metabolism and ion dynamics

The detailed explanation of the mathematical expressions and parameters of the model were previously presented in Wei et al. (2011).

Computational modeling of Na⁺/H⁺ exchanger (NHE) and phosphate carrier (PiC)

$$J_{NHE} = c_{NHE} \frac{\dfrac{\beta_1^+ \beta_2^+ - \beta_1^- \beta_2^-}{\beta_1^+ + \beta_1^- + \beta_2^+ + \beta_2^-}}{1 + 10^{n_i (pH_i - pK_i)}}$$

where

$$\beta_1^+ = \frac{k_1^+ K_{H\_NHE} [Na^+]_m}{K_{H\_NHE} [Na^+]_m + K_{H\_NHE} K_{Na\_NHE} + K_{Na\_NHE} [H^+]_m}$$

$$\beta_2^+ = \frac{k_4^+ K_{Na\_NHE} [H^+]_i}{K_{H\_NHE} [Na^+]_i + K_{H\_NHE} K_{Na\_NHE} + K_{Na\_NHE} [H^+]_i}$$

$$\beta_1^- = \frac{k_1^- K_{H\_NHE} [Na^+]_i}{K_{H\_NHE} [Na^+]_i + K_{H\_NHE} K_{Na\_NHE} + K_{Na\_NHE} [H^+]_i}$$

$$\beta_2^- = \frac{k_4^- K_{Na\_NHE} [H^+]_m}{K_{H\_NHE} [Na^+]_m + K_{H\_NHE} K_{Na\_NHE} + K_{Na\_NHE} [H^+]_m}$$

$$J_{PIC} = c_{PiC} \frac{V_{PIC,f} \dfrac{[H_2PO_4^{2-}]_i [OH^-]_m}{K_{Pi,i} K_{OH,m}} - V_{PIC,b} \dfrac{[H_2PO_4^{2-}]_m [OH^-]_i}{K_{Pi,m} K_{OH,i}}}{\left(1 + \dfrac{[H_2PO_4^{2-}{}_i}{K_{Pi,i}} + \dfrac{[OH^-]_m}{K_{OH,m}} + \dfrac{[H_2PO_4^{2-}]_m}{K_{Pi,m}} + \dfrac{[OH^-]_i}{K_{OH,i}} + \dfrac{[H_2PO_4^{2-}]_m [OH^-]_i}{K_{Pi,m} K_{OH,i}} + \dfrac{[H_2PO_4^{2-}]_i [OH^-]_m}{K_{Pi,i} K_{OH,m}}\right)}$$

Table S6 Parameter values for the mitochondrial Na+/H+ proton exchanger and phosphate carrier – mitochondrial and cellular models

Symbol	Value	Units	Description	Reference
k_1^+	0.0252	ms^{-1}	NHE forward rate constant	(2)
k_1^-	0.0429	ms^{-1}	NHE backward rate constant	(2)
k_4^+	0.16	ms^{-1}	NHE forward rate constant	(2)
k_4^-	0.0939	ms^{-1}	NHE backward rate constant	(2)
K_{Na_NHE}	24	mM	Na+Dissociation constant	(2)
K_{H_NHE}	1.585×10^{-4}	mM	H+Dissociation constant	(2)
pK_i	8.52		Proton inhibitory constant	(2)
n_i_NHE	3		Hill coefficient for H+ binding	(2)
c_{NHE}	0.00785 (mitochondria)	mM	NHE concentration	(2)
$K_{Pi,i}$	11.06	mM	Extra-matrix Pi binding constant	(2)
$K_{Pi,m}$	11.06	mM	Mitochondrial matrix Pi binding constant	(2)
$K_{OH,i}$	4.08×10^{-5}	mM	Extra-matrix OH- binding constant	(2)
$K_{OH,m}$	4.08×10^{-5}	mM	Mitochondrial matrix OH- binding constant	(2)
$V_{PIC,f}$	90	µmol min^{-1} mg $protein^{-1}$	Forward V_{max}	(2)
$V_{PIC,b}$	90	µmol min^{-1} mg $protein^{-1}$	Backward V_{max}	(2)
c_{PiC}	4.9	mg protein ml^{-1}	PiC concentration	Adjusted

TCA cycle rate equations

$$\mathrm{V_{CS}} = \frac{\mathrm{k_{cat}^{CS}\ E_T^{CS}}}{\left(1+\dfrac{\mathrm{K_M^{AcCoA}}}{\mathrm{[AcCoA]}}\right)\left(1+\dfrac{\mathrm{K_M^{OAA}}}{\mathrm{[OAA]}}\right)}$$

$$\mathrm{V_{ACO}} = \mathrm{k_f^{ACO}} \left(\mathrm{[CIT]} - \frac{\mathrm{[ISOC]}}{\mathrm{K_E^{ACO}}} \right)$$

$$V_{IDH} = k_{cat}^{IDH} E_T^{IDH} \left[\begin{array}{l} \left(1 + \frac{[H^+]_m}{k_{h,1}} + \frac{k_{h,2}}{[H^+]_m} \right) + f_i^{IDH} \left(\frac{K_{Midh}^{NAD}}{[NAD]} \right) + \ldots \\ f_a^{IDH} \left(\frac{K_M^{ISOC}}{[ISOC]} \right)^{ni} + f_a^{IDH} f_i^{IDH} \left(\frac{K_M^{ISOC}}{[ISOC]} \right)^{ni} \left(\frac{K_{Midh}^{NAD}}{[NAD]} \right) \end{array} \right]^{-1}$$

$$f_a^{IDH} = \left[\left(1 + \frac{[ADP^{3-}]_m}{K_{ADP}^a} \right) \left(1 + \frac{[Ca^{2+}]_m}{K_{Ca}^a} \right) \right]^{-1}$$

$$f_i^{IDH} = \left(1 + \frac{[NADH]}{K_{i,NADH}} \right)$$

$$V_{KGDH} = \frac{k_{cat}^{KGDH} E_T^{KGDH}}{1 + \frac{[H^+]_m}{k_{h,1a}} + \frac{k_{h,2a}}{[H^+]_m} + f_a^{KGDH} \left(\frac{k_M^{\alpha KG}}{[\alpha KG]} \right)^{n_{\alpha KG}} + f_a^{KGDH} \frac{k_{M\_kgdh}^{NAD}}{[NAD]}}$$

$$f_a^{KGDH} = \left[\left(1 + \frac{[Mg^{2+}]}{K_D^{Mg^{2+}}} \right) \left(1 + \frac{[Ca^{2+}]_m}{K_D^{Ca^{2+}}} \right) \right]^{-1}$$

$$V_{SL} = k_f^{SL} \left([SCoA][ADP]_m[Pi]_m - \frac{[Suc][ATP]_m[CoA]}{K_{E,app}^{SL}} \right)$$

$$K_{E,app}^{SL} = K_{Eq}^{SL} \frac{P_{SUC} P_{ATP}}{P_{Pi} P_{ADP}}$$

Succinate dehydrogenase is included in the Table comprising the respiratory complexes

$$V_{FH} = k_f^{FH} \left([FUM] - \frac{[MAL]}{K_E^{FH}} \right)$$

$$V_{MDH} = \frac{k_{cat}^{MDH} E_T^{MDH} f_{h,a} f_{h,i}}{1 + \frac{K_M^{MAL}}{[MAL]} \left(1 + \frac{[OAA]}{K_i^{OAA}} \right) + \frac{K_M^{NAD}}{[NAD]} + \frac{K_M^{MAL}}{[MAL]} \left(1 + \frac{[OAA]}{K_i^{OAA}} \right) \frac{K_M^{NAD}}{[NAD]}}$$

$$f_{h,a} = \left(1 + \frac{[H^+]}{k_{h1}} + \frac{[H^+]^2}{k_{h1}k_{h2}}\right)^{-1} + k_{offset}$$

$$f_{h,i} = \left(1 + \frac{k_{h3}}{[H^+]} + \frac{k_{h3}k_{h4}}{[H^+]^2}\right)$$

$$V_{AAT} = k_f^{AAT}[OAA][GLU]\frac{k_{ASP}K_E^{ATT}}{\left(k_{ASP}K_E^{AAT} + [\alpha KG]k_f^{AAT}\right)}$$

Table 7 Parameter values used in the simulations: Tricarboxylic acid cycle -- mitochondrial model

Symbol	Value	Units	Description	Reference
[AcCoA]	1×10^{-5}-1	mM	Acetyl CoA concentration	(2)
k_{cat}^{CS}	2.3523×10^{-4}	ms^{-1}	Catalytic constant of CS	(2)*
E_T^{CS}	0.4	mM	Concentration of CS	(2)
K_M^{AcCoA}	0.0126	mM	Michaelis constant for AcCoA	(2)
K_M^{OAA}	6.4×10^{-4}	mM	Michaelis constant for OAA	(2)
$C_{k\,\mathrm{int}}$	1.3	mM	Sum of TCA cycle intermediates	(2)
k_f^{ACO}	1.1688×10^{-4}	ms^{-1}	Forward rate constant of ACO	(2)*
K_E^{ACO}	2.22		Equilibrium constant of ACO	(2)
$K_{i,NADH}$	0.19	mM	Inhibition constant by NADH	(2)
k_{cat}^{IDH}	11.88	ms^{-1}	Rate constant of IDH	(2)*
E_T^{IDH}	0.109	mM	Concentration of IDH	(2)
$k_{h,1}$	1×10^{-5}	mM	Inoization constant of IDH	(2)
$k_{h,2}$	9×10^{-4}	mM	Inoization constant of IDH	(2)
K_M^{ISOC}	1.52	mM	Michaelis constant for isocitrate	(2)
n_i	2.0		Cooperativity for isocitrate	(2)

K_{Midh}^{NAD}	0.923	mM	Michaelis constant for NAD^{+}	(2)
K_{ADP}^{a}	0.62	mM	Activation constant by ADP	(2)
K_{Ca}^{a}	5×10^{-4}	mM	IDH activation constant for Ca^{2+}	(2)
E_{T}^{KGDH}	0.5	mM	Concentration of KGDH	(2)
k_{cat}^{KDGH}	0.0132	ms^{-1}	Rate constant of KGDH	(2)*
$k_{M}^{\alpha KG}$	30	mM	Michaelis constant for αKG	(2)
$K_{M\_kgdh}^{NAD}$	38.7	mM	Michaelis constant for NAD^{+} of KGDH	(2)
$k_{h,1a}$	4×10^{-5}	mM	Ionization constant of KGDH	(2)
$k_{h,2a}$	7×10^{-5}	mM	Ionization constant of KGDH	(2)
$K_{D}^{Mg^{2+}}$	0.0308	mM	Activation constant for Mg^{2+}	(2)
$K_{D}^{Ca^{2+}}$	1.5×10^{-4}	mM	Activation constant for Ca^{2+}	(2)
$n_{\alpha KG}$	1.2		Hill coefficient of KGDH for α KG	(2)
$[Mg^{2+}]_{m}$	0.4	mM	Mg^{2+} concentration in mitochondria	(2)
$[Mg^{2+}]_{i}$	1.0	mM	Mg^{2+} concentration in cytosol/buffer	(2)
k_{f}^{SL}	0.028	mM^{-1}ms^{-1}	Forward rate constant of SL	(2)*
K_{E}^{SL}	3.115		Equilibrium constant of the SL reaction	(2)
[CoA]	0.02	mM	Coenzyme A concentrations.	(2)
k_{f}^{FH}	8.3×10^{-3}	ms^{-1}	Forward rate constant for FH.	(2)*
K_{E}^{FH}	1.0		Equilibrium constant of FH	(2)
k_{h1}	1.131×10^{-5}	mM	Ionization constant of MDH	(2)

k_{h2}	26.7	mM	Ionization constant of MDH	(2)
k_{h3}	6.68×10^{-9}	mM	Ionization constant of MDH	(2)
k_{h4}	5.62×10^{-6}	mM	Ionization constant of MDH	(2)
k_{offset}	3.99×10^{-2}		Offset of MDH pH activation factor	(2)
k_{cat}^{MDH}	0.1242	ms^{-1}	Rate constant of MDH	(2)*
E_T^{MDH}	0.154	mM	Total MDH enzyme concentration	(2)
K_M^{MAL}	1.493	mM	Michaelis constant for malate	(2)
K_i^{OAA}	0.031	mM	Inhibition constant for oxaloacetate	(2)
K_M^{NAD}	0.2244	mM	Michaelis constant for NAD^+	(2)
[GLU]	1×10^{-5} - 30	mM	Glutamate concentration.	(2)
k_f^{AAT}	0.0214	ms^{-1}	Forward rate constant of AAT	(2)*
K_E^{AAT}	6.6		Equilibrium constant of AAT	(2)
k_{ASP}	1.5×10^{-6}	ms^{-1}	Rate constant of aspartate consumption	(2)

*While these parameters may differ from the supplement of Kembro et al., they were taken from code provided by those authors that successfully reproduces the figures from the paper.

Table 8 Parameter values used in the simulations: Tricarboxylic acid cycle -- mitochondrial model

Symbol	Value	Units	Description	Reference
[AcCoA]	1	mM	Acetyl CoA concentration	(2)
k_{cat}^{CS}	1.5891×10^{-4}	ms^{-1}	Catalytic constant of CS	(2)*
k_f^{ACO}	7.8959×10^{-5}	ms^{-1}	Forward rate constant of ACO	(2)*
k_{cat}^{IDH}	0.5350	ms^{-1}	Rate constant of IDH	(2)*

k_{cat}^{KDGH}	0.0179	ms^{-1}	Rate constant of KGDH	(2)*
k_{f}^{SL}	0.0284	$mM^{-1}ms^{-1}$	Forward rate constant of SL	(2)*
k_{f}^{FH}	8.4×10^{-3}	ms^{-1}	Forward rate constant for FH.	(2)*
k_{cat}^{MDH}	0.1259	ms^{-1}	Rate constant of MDH	(2)*
[GLU]	30	mM	Glutamate concentration.	(2)
k_{f}^{AAT}	0.0217	ms^{-1}	Forward rate constant of AAT	(2)*

Oxidative phosphorylation equations for the mitochondrial model are the same as for Gauthier et al. (14) with the exception of k_{010}, which was increased from 50 to 600 to match experimental data from Aon et al. 2012 (1) on ROS production from isolated mitochondria. Rate constants were scaled to yield fluxes in /ms units. Parameter changes for the cellular model are noted below.

Table 9 Parameter values used in the simulations: electron transport chain -- cellular model

Symbol	Value	Units	Description	Reference
ρ_{c1}	24.9302	mM	Complex I concentration	Adjusted
a_{61}*	3.3290×10^{7}	mM/s		Adjusted
a_{16}*	432.7642	mM/s		Adjusted
k_{010}	1700	mM/min	Reverse reaction constant for reduction of oxygen by SQ_p	Adjusted

Table 10 Parameter values used in the simulations: oxidative phosphorylation -- mitochondrial model

Symbol	Value	Units	Description	Reference
p_1	1.346×10^{-4}		Sum of products of rate constants	
p_2	7.739×10^{-7}		Sum of products of rate constants	
p_3	6.65×10^{-15}		Sum of products of rate constants	
ρ^{F1}	5	mM	Concentration of F_1F_0-ATPase	(2)

K_{eq}^{ATPase}	1.71×10^{6}		Equilibrium constant of ATP synthesis	
$[\mathrm{Pi}]_i$	3	mM	Inorganic phosphate concentration	
C_A	1.01	mM	Total sum of adenine nucleotides	(2)*
V_{maxANT}	3.15	mM ms^{-1}	Maximal rate of the ANT	(2)
h^{ANT}	0.5		Fraction of $\Delta\Psi_B$	
g_H	2×10^{-6}	mM ms^{-1} mV^{-1}	Ionic conductance of the inner membrane	(2)
C_{PN}	1.0	mM	Total sum of pyridine nucleotides	
C_{mito}	1.812×10^{-3}	mM mV^{-1}	Inner membrane capacitance	

Table 11 Parameter values used in the simulations: oxidative phosphorylation -- cellular model

Symbol	Value	Units	Description	Reference
ρ^{F1}	5	mM	Concentration of F_1F_0-ATPase	Adjusted

Table 12 Parameter values used in the simulations: Mitochondrial Ca^{2+} handling – mitochondrial model

Symbol	Value	Units	Description
$V_{\max}^{uni}$	4.46×10^{-3}	mM ms^{-1}	V_{max}uniporter Ca^{2+} transport
$\Delta\Psi^{\circ}$	91	mV	Offset membrane potential
K_{act}	3.8×10^{-4}	mM	Activation constant
K_{trans}	0.019	mM	K_d for translocated Ca^{2+}
L	110.0		K_{eq} for conformational transitions in uniporter
n_a	2.8		Uniporter activation cooperativity
$V_{\max}^{NaCa}$	1.83×10^{-4}	mM ms^{-1}	V_{max} of Na^+/Ca^{2+} exchanger
b	0.5		$\Delta\Psi_m$ dependence on Na^+/Ca^{2+} exchanger

K_{Na}	9.4	mM	Exchanger Na^{2+} constant
K_{Ca}	3.75×10^{-4}	mM	Exchanger Ca^{2+} constant
n	3.0		Na^+/Ca^{2+} exchanger cooperativity
δ_{Ca}	3×10^{-4}		Fraction of free $[Ca^{2+}]_m$

Table 13 Parameter values used in the simulations: Mitochondrial Ca^{2+} handling – cellular model

Symbol	Value	Units	Description	Reference
$V_{\max}^{uni}$	1.2295×10^{-4}	mM ms^{-1}	V_{max} uniporter Ca^{2+} transport	Adjusted
$V_{\max}^{NaCa}$	4.6650×10^{-5}	mM ms^{-1}	V_{max} of Na^+/Ca^{2+} exchanger	Adjusted

For Ru360 protocols, Vuni was 99% blocked. For CGP protocols, VNaCa was 85% blocked.

Table 14 Parameter values used in the simulations: Mitochondrial H^+ and Na^+ handling – mitochondrial model

Symbol	Value	Units	Description	Reference
δ_H	1×10^{-5}	dimensionless	mitochondria H^+ buffering capacity	(2)
$K_{a,ADP}$	4.17×10^{-7}		ADP dissociation constant	(2)
$K_{a,ATP}$	3.31×10^{-7}		ATP dissociation constant	(2)
$K_{a,Pi}$	1.78×10^{-7}		Pi dissociation constant	(2)
$K_{Mg,ATP}$	6.46×10^{-5}		Mg^{2+}ATP dissociation constant	(2)
$K_{Mg,ADP}$	5.62×10^{-4}		Mg^{2+}ADP dissociation constant	(2)
$K_{a,SUC}$	6.3×10^{-6}		Ka of succinate dissociation constant	(2)
K_{a,H_2O}	1×10^{-14}	M	dissociation constant for water	(2)
$[H^+]_i$	1×10^{-4}	mM	cytosolic H^+ concentration	(2)
$[Na^+]_i$	10	mM	cytosolic Na^+ concentration	(2)*
$[Ca^{2+}]_i$	1×10^{-4}	mM	cytosolic Ca^{2+} concentration	(2)
$[ADP]_i$	0.01~1.0	mM	cytosolic ADP concentration	(2)

Table 15 Parameter values used in the simulations: Mitochondrial H^+ and Na^+ handling – cellular model

Symbol	Value	Units	Description	Reference
$[Na^+]_i$	5-15	mM	cytosolic Na^+ concentration	(15)
$[Ca^{2+}]_i$	1×10^{-4}	mM	diastolic cytosolic Ca^{2+} concentration	(2)

Control Nai is 5mM, heart failure simulations used 15mM.

Table 16 Parameter values used in the simulations: ROS transport – mitochondrial and cellular models

Symbol	Value	Units	Description	Reference
a	1×10^{-3}	dimensionless	Basal IMAC conductance	(2)
b	1×10^{4}	dimensionless	Activation factor by cytoplasmic $O_2^{\cdot-}$	(2)
K_{cc}	1×10^{-2}	mM	Activation constant by cytoplasmic $O_2^{\cdot-}$	(2)
GL	3.5×10^{-8}		Integral conductance for IMAC	(2)
G_{max}	3.9085×10^{-6}		Leak conductance of IMAC at saturation	(2)
K	7.0×10^{-2}	mV^{-1}	Steepness factor	(2)
$\Delta\Psi_m^b$	4	mV	Potential at half saturation	(2)
j	0.1	dimensionless	Fraction of IMAC conductance	(2)
$\frac{RT}{F}$	26.730818			(2)

1. Aon, M. A., B. A. Stanley, V. Sivakumaran, J. M. Kembro, B. O'Rourke, N. Paolocci, and S. Cortassa. 2012. Glutathione/thioredoxin systems modulate mitochondrial H2O2 emission: An experimental-computational study. The Journal of general physiology 139:479-491.
2. Kembro, J. M., M. A. Aon, R. L. Winslow, B. O'Rourke, and S. Cortassa. 2013. Integrating Mitochondrial Energetics, Redox and ROS Metabolic Networks: A Two-Compartment Model. Biophysical journal 104:332-343.

3. Cortassa, S., M. A. Aon, R. L. Winslow, and B. O'Rourke. 2004. A mitochondrial oscillator dependent on reactive oxygen species. Biophysical journal 87:2060-2073.
4. Fernandes, A. P., and A. Holmgren. 2004. Glutaredoxins: glutathione-dependent redox enzymes with functions far beyond a simple thioredoxin backup system. Antioxidants & redox signaling 6:63-74.
5. Holmgren, A. 1989. Thioredoxin and glutaredoxin systems. J Biol Chem 264:13963-13966.
6. Cox, A. G., C. C. Winterbourn, and M. B. Hampton. 2010. Mitochondrial peroxiredoxin involvement in antioxidant defence and redox signalling. Biochem J 425:313-325.
7. Sztajer, H., B. Gamain, K. D. Aumann, C. Slomianny, K. Becker, R. Brigelius-Flohe, and L. Flohe. 2001. The putative glutathione peroxidase gene of Plasmodium falciparum codes for a thioredoxin peroxidase. J Biol Chem 276:7397-7403.
8. Pillay, C. S., J. H. Hofmeyr, B. G. Olivier, J. L. Snoep, and J. M. Rohwer. 2009. Enzymes or redox couples? The kinetics of thioredoxin and glutaredoxin reactions in a systems biology context. Biochem J 417:269-275.
9. Eckenroth, B., K. Harris, A. A. Turanov, V. N. Gladyshev, R. T. Raines, and R. J. Hondal. 2006. Semisynthesis and characterization of mammalian thioredoxin reductase. Biochemistry 45:5158-5170.
10. Carlberg, I., and B. Mannervik. 1984. Glutathione reductase. Methods in enzymology 113:484-490.
11. Zhou, L., S. Cortassa, A.-C. Wei, M. A. Aon, R. L. Winslow, and B. O'Rourke. 2009. Modeling Cardiac Action Potential Shortening Driven by Oxidative Stress-Induced Mitochondrial Oscillations in Guinea Pig Cardiomyocytes. Biophysical journal 97:1843-1852.
12. Popova, T., M. A. Carvalho, L. Matasova, and L. Medvedeva. 2007. Regulation of mitochondrial NADP-isocitrate dehydrogenase in rat heart during ischemia. Molecular and Cellular Biochemistry 294:97-105.
13. Sazanov, L. A., and J. B. Jackson. 1994. Proton-translocating transhydrogenase and NAD- and NADP-linked isocitrate dehydrogenases operate in a substrate cycle which contributes to fine regulation of the tricarboxylic acid cycle activity in mitochondria. FEBS Letters 344:109-116.
14. Gauthier, L. D., J. L. Greenstein, S. Cortassa, B. O'Rourke, and R. L. Winslow. 2013. A Computational Model of Reactive Oxygen Species and Redox Balance in Cardiac Mitochondria. Biophysical Journal 105:1045-1056.
15. Kohlhaas, M., T. Liu, A. Knopp, T. Zeller, M. F. Ong, M. Böhm, B. O'Rourke, and C. Maack. 2010. Elevated cytosolic Na+ increases mitochondrial formation of reactive oxygen species in failing cardiac myocytes. Circulation 121:1606-1613.